Eur. Phys. J. D **7**, 289–309 (1999)

THE EUROPEAN PHYSICAL JOURNAL D

EDP Sciences

Buffer-gas loaded magnetic traps for atoms and molecules: A primer

R. deCarvalho[1], J.M. Doyle[1,a], B. Friedrich[1,2,b], T. Guillet[1], J. Kim[1], D. Patterson[1], and J.D. Weinstein[1]

[1] Department of Physics, Harvard University, Cambridge, MA 02138, USA
[2] Department of Chemistry and Chemical Biology, Harvard University, Cambridge, MA 02138, USA

Received 2 November 1998 and Received in final form 19 February 1999

Abstract. Over the past three years we have developed the technique of buffer-gas cooling and loading of atoms and molecules into magnetic traps. Buffer-gas cooling relies solely on elastic collisions (thermalization) of the species-to-be-trapped with a cryogenically cooled helium gas and so is independent of any particular energy level pattern. This makes the cooling technique general and potentially applicable to any species trappable at the temperature of the buffer gas (as low as 240 mK). Using buffer-gas loading, paramagnetic atoms (europium and chromium) as well as a molecule (calcium monohydride) were trapped at temperatures around 300 mK. The numbers of the trapped atoms and molecules were respectively about 10^{12} and 10^8. The atoms and molecules were produced by laser ablation of suitable solid precursors. In conjunction with evaporative cooling, buffer-gas loaded magnetic traps offer the means to further lower the temperature and increase the density of the trapped ensemble to study a large variety of both static (spectra) and dynamic (collisional cross-sections) properties of many atoms and molecules at ultra-low temperatures. In this article we survey our main results obtained on Cr, Eu, and CaH and outline prospects for future work.

PACS. 32.80.Pj Optical cooling of atoms; trapping – 06.30.Ft Time and frequency – 32.30.Jc Visible and ultraviolet spectra

1 Introduction

The very low temperatures ($\leq 1\ \mu$K) and simultaneously high densities ($\geq 10^{14}$ cm^{-3}) attainable with magnetic trapping and evaporative cooling techniques have enabled a number of experiments with atoms whose de Broglie wavelengths are on the order of, or larger than, the mean distance between the atoms. Often these wavelengths are larger than that of visible light. Work based on evaporative cooling [1] has in the past relied on photon scattering to precool the atoms (with the unique, notable, exception of atomic hydrogen). The applicability of optical cooling has, in turn, limited the scope of species that could be explored in the ultracold regime primarily to the alkali metal atoms. Molecules and the vast majority of atomic species have been relegated to the sidelines. In order for the full impact of the cooling techniques to be realized, a more general approach is required. Ideally, the desire for a particular ultracold atomic or molecular species would be matched by a straightforward production method, whose generality would be comparable to that of the atomic or molecular beam methods developed through the 1960's.

Over the past three years we have developed a cooling technique that is applicable to a wide range of species, including molecules. This new technique relies on thermalization with a cold He buffer gas *via* elastic collisions. The collisional cross-section of atoms and molecules with He is independent of any particular energy level pattern and can increase with decreasing temperature, thus lending the technique the desired generality and efficiency.

In our work, we combined buffer-gas cooling with magnetic trapping. First we demonstrated the technique by buffer-gas loading atomic europium (with a maximum dipole moment of 7 Bohr magnetons) into a magnetic trap. This work corroborated the feasibility of the scheme and produced the first benefits of magnetic trapping of a complex atom: a hyperfine-resolved Zeeman spectrum whose variation with time provided clues about the relaxation dynamics of the trapped states. About 10^{12} Eu atoms were trapped.

Next, we buffer gas loaded isotopically pure chromium atoms, ^{52}Cr (a 6 Bohr magneton species). Like the Eu atoms, Cr atoms were prepared by laser ablation of a solid metal precursor. The study of the time dependence of the simple Zeeman spectra (no hyperfine structure) led us to the discovery of an important variant of the buffer-gas loading technique, termed "cold loading": the condensed buffer gas itself can be efficiently vaporized by the same laser pulse that is used to ablate the metal.

[a] e-mail: jd@jsbach.harvard.edu
[b] e-mail: brich@chemistry.harvard.edu

More than 10^{11} Cr atoms were trapped using either normal or cold loading.

The work on Eu and Cr trapping makes us believe that it is possible to use buffer-gas loading to magnetically trap all paramagnetic atoms of the periodic table of elements. Figure 1 shows a rendition of the periodic table of elements that emphasizes features which are of particular interest in atom trapping. Note that the following elements have maximum magnetic moments of 5 Bohr magnetons or greater: Mn, Re, Tc, Mo, Cr, Eu, Gd, Fe, Os, Ni, Co, Rh, Ir, Ru, Er, Tb, Ho, and Dy [2,3]. Such magnetic moments can lead to high trap depths, making these atoms prime candidates for future work, perhaps using a table-top liquid-helium cooled apparatus.

Our efforts culminated in the first trapping of a molecule, CaH. The molecules (with a magnetic dipole moment of 1 Bohr magneton) were prepared by laser ablation of a solid CaH_2 precursor. About 10^8 were loaded using ^{3}He-buffer into an anti-Helmholtz magnetic trap. Detailed, time dependent Zeeman spectra were measured using laser induced fluorescence spectroscopy. These spectra provided insights into both the trapping dynamics and the electronic structure of CaH.

In this paper we give a guided tour of the main results obtained so far with buffer-gas loaded magnetic traps.

2 Buffer-gas loaded magnetic traps

2.1 Principle

The technique of buffer-gas loading [3] relies on thermalization of the species-to-be-trapped *via* collisions with a cold buffer gas. The buffer gas serves to dissipate the translational energy of the atoms or molecules, allowing them to sink into a conservative trapping field. Since this dissipation scheme does not depend on any particular energy level pattern, many atoms and molecules are amenable to it. As in the case of evaporative cooling of a trapped ensemble, buffer gas loading relies on elastic collisions and, therefore, is of similar generality.

At temperatures of $\sim$ 1 K, all stable substances except for He have negligible vapor pressure, so the question arises as to how to bring the species-to-be-trapped into the gas phase. We found that laser ablation represents a particularly suitable means, although not the only one. Metal atoms can be efficiently vaporized by ablating a piece of solid metal; it is also possible to "prepare" molecules, of varying complexity, by ablating a suitable precursor [4]. In what follows we assume that the atoms or molecules are introduced into the gas phase by laser ablation.

The thermalization process can be modelled by assuming elastic collisions between two mass points, m (buffer-gas atom) and M (species-to-be-trapped). From energy and momentum conservation in a hard-sphere model, we find, after thermal averaging, that the difference, ΔT, in temperature of the atom or molecule before and after a collision with the buffer gas atom is given by $\Delta T = (T' - T)/\kappa$, with T the temperature of the buffer gas, T' the initial temperature of the atom or molecule, and

$$\kappa \equiv (M + m)^2/(2Mm). \tag{1}$$

The equation for the temperature change can be generalized and recast in differential form:

$$\mathrm{d}T_\ell/\mathrm{d}\ell = -(T_\ell - T)/\kappa \tag{2}$$

where T_ℓ is the temperature of the atom or molecule after ℓ collisions with the buffer gas atom. Equation (2) has a solution

$$T_\ell/T = (T'/T - 1)\exp(-\ell/\kappa) + 1. \tag{3}$$

Under the conditions of $T' \approx 1000$ K and $M/m \approx 50$, on the order of one hundred collisions are required for the atoms or molecules to fall within 30% of the He buffer temperature $T = 0.25$ K. In order to ensure that the atoms or molecules thermalize before impinging on the wall of the cell surrounding the trap (where, presumably, they would stick and be lost), it is necessary that the density of the buffer gas be large enough to allow for thermalization on a path smaller than the size of the cell (*i.e.* on the order of 1 cm). Assuming an elastic collision cross-section of about 10^{-14} cm^2 between the atoms or molecules and ^{3}He, the minimum density required is on the order of 10^{16} cm^{-3}. This requirement puts a lower limit on the temperature of the buffer gas. Figure 2 shows the dependence of number density on temperature for ^{3}He and ^{4}He at about 1 K [5,6]. One can see that ^{3}He (which has the highest number density of any stable substance at low temperatures) is suitable at temperatures as low as 240 mK.

Buffer-gas cooling combines naturally with magnetic traps as both the loading and the trapping techniques make use of cryogenics. In what follows we consider a static magnetic trapping field whose field strength $\mathcal{H}$ increases linearly with distance r from $\mathcal{H}(r = 0) = 0$ at the center up to $\mathcal{H}(r = r_{\mathrm{edge}}) = \mathcal{H}_{\mathrm{edge}}$ at the edge of the trap. Such an inhomogeneous field deflects paramagnetic species in low-field seeking states (*i.e.* states whose eigenenergy increases with increasing field strength) towards the minimum at its center and species in the high-field seeking states (whose eigenenergy decreases with increasing field strength) towards the maximum at its edge. The presence of a process such as buffer-gas cooling, which dissipates the translational energy of the paramagnetic species, can then lead to trapping: this ultimately occurs when the translational energy of the atoms or molecules in low-field seeking states falls below the value of the magnetic dipole potential at the trap edge. The number density of a trapped paramagnetic species follows a Boltzmann distribution

$$n(r) = n_0 \mathrm{e}^{-\gamma(r)} \tag{4}$$

with

$$\gamma(r) \equiv \frac{\langle\mu\rangle\mathcal{H}(r)}{kT} \geq 0 \tag{5}$$

where $\langle\mu\rangle$ is the expectation value of the space-fixed magnetic dipole moment pertaining to a low-field seeking state

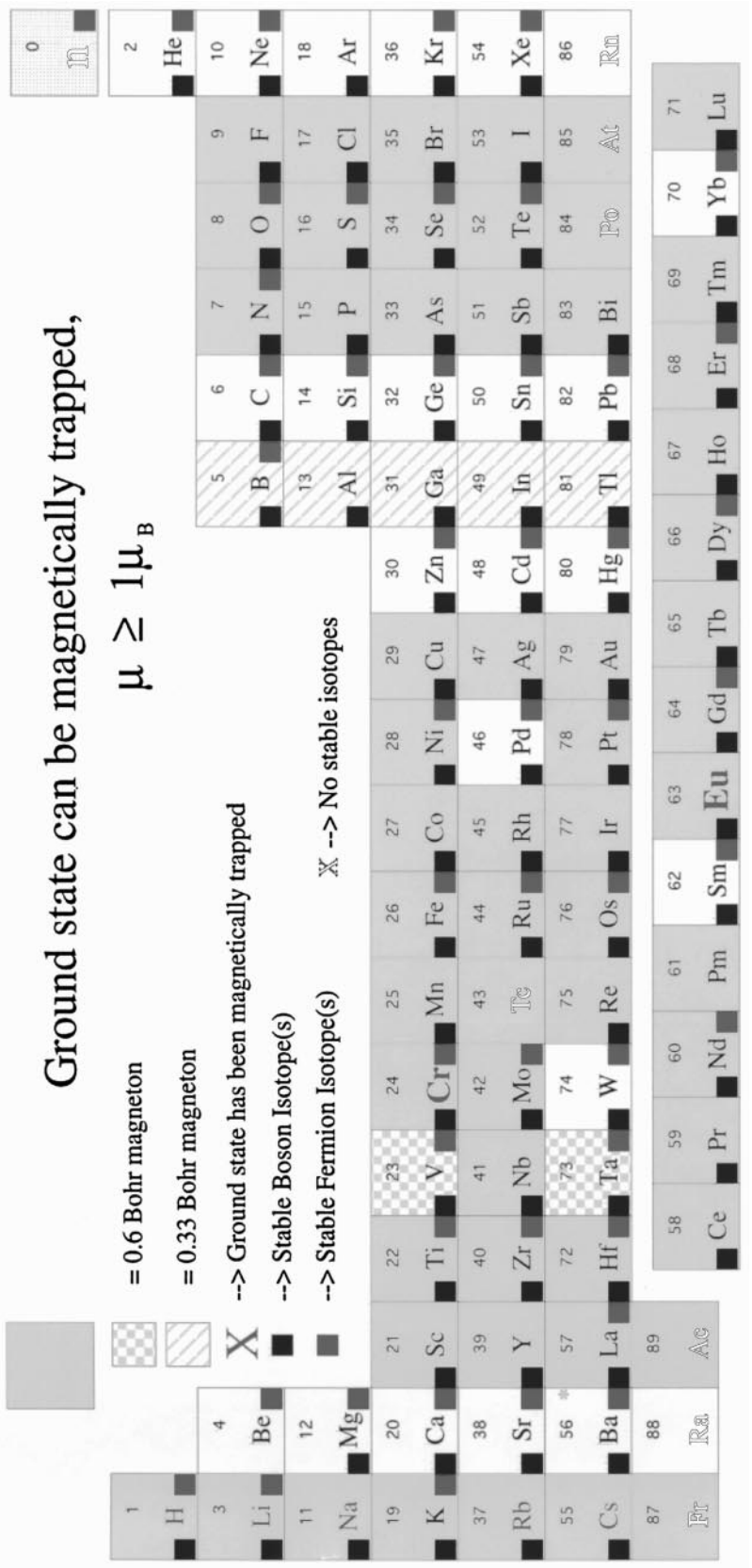

Fig. 1. A rendition of the periodic table of elements adapted to atomic trapping. Paramagnetic elements are in grey fields. Black and dark-grey squares designate respectively stable bosonic and fermionic isotopes.

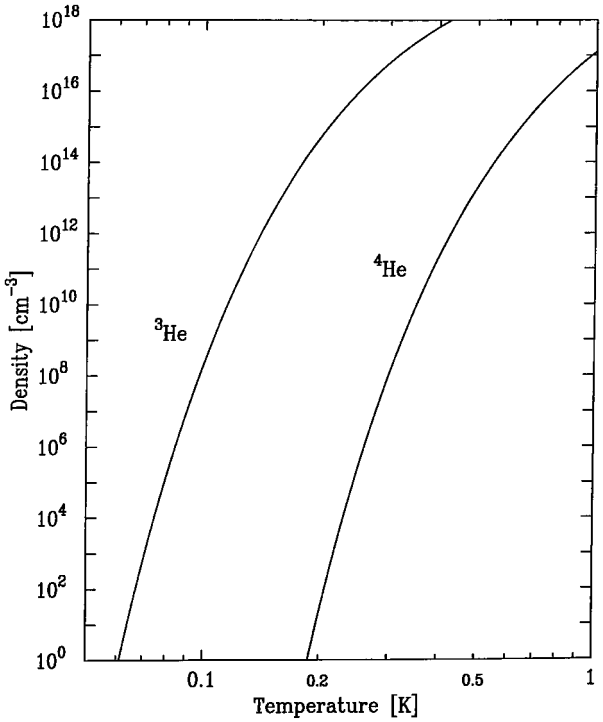

Fig. 2. Low-temperature number density curves of ^{3}He and ^{4}He. Note that the minimum number density of about 10^{16} cm^{-3} required for buffer-gas loading is attained at 240 mK in ^{3}He and 800 mK in ^{4}He.

of the species, T its translational temperature, and k the Boltzmann constant; $n_0 \equiv n(r = 0)$ is the (maximum) density at the center of the trap. The total number, N, of trapped atoms or molecules is related to n_0 by

$$N = n_0 V \tag{6}$$

where V is the *effective volume* of the trap. The effective volume is determined by the temperature of the atoms or molecules and the geometry of the trapping field. For the spherical field considered (diameter of 5 cm and $\mathcal{H}_{\rm edge} = 3$ T), a model calculation yields $V = V_0 \eta^{-3}$ with $V_0 = 390$ cm^3 and $\eta \equiv \gamma_{\rm edge}$. This is sufficiently accurate for $\eta > 5$ [7]. The loss rate, $\dot{N}$, over the edge of the trap is given by

$$\dot{N} = \frac{1}{4} v n A \equiv \frac{1}{4} v n_0 A_{\rm eff} \tag{7}$$

with v the average speed of the atoms or molecules and

$$A_{\rm eff} = \iint_{\rm edge} {\rm e}^{-\gamma(r)} {\rm d}^2 r \tag{8}$$

an effective trap surface area. The combination of equations (6, 7) yields the lifetime of the atoms or molecules in the trap (in the absence of any other loss mechanism):

$$\tau = \frac{N}{\dot{N}} = \frac{4 V_0}{A_{\rm eff} v \eta^3} \,. \tag{9}$$

This lifetime can be reduced by other trap loss mechanisms such as dipolar relaxation [1] and Majorana transitions [8].

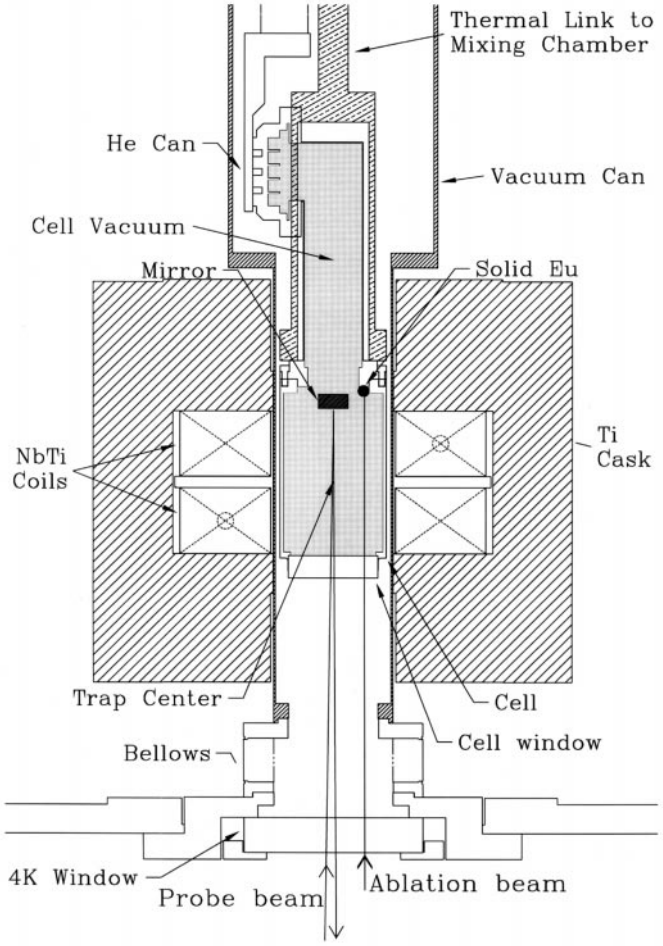

Fig. 3. Schematic diagram of magnetic trapping apparatus. The copper cell, located in the bore of a superconducting magnet, is anchored to the mixing chamber of a dilution refrigerator. The magnet is immersed in liquid helium. Optical access to room temperature is provided by a fused silica window at the bottom of the cell and a set of borosilicate windows at 4, 77, and 300 K. Only the cell and the 4 K windows are shown. The remaining windows lie directly underneath.

2.2 Apparatus

The cross-section of the cryogenic apparatus we have used in our experiments is depicted in Figure 3. The apparatus consists of three main parts: the superconducting magnet, the cryogenic cell, and the dilution refrigerator. The magnet (5.1 cm clear bore) consists of two NbTi superconducting solenoids encased in a titanium cask. The two coils are arranged in the anti-Helmholtz configuration and therefore repel each other. The repulsive force (of up to about 10^5 N) is taken up by the cask. The individual solenoids are both 2.8 cm thick with an inner and outer diameter of 5.3 and 13.0 cm, respectively. Their centers are separated by 3.3 cm. The entire magnet assembly is immersed in liquid helium.

The cell is positioned at the center of the magnet. It resides in vacuum and is separated from the magnet (and the liquid helium) by a stainless steel vacuum can,

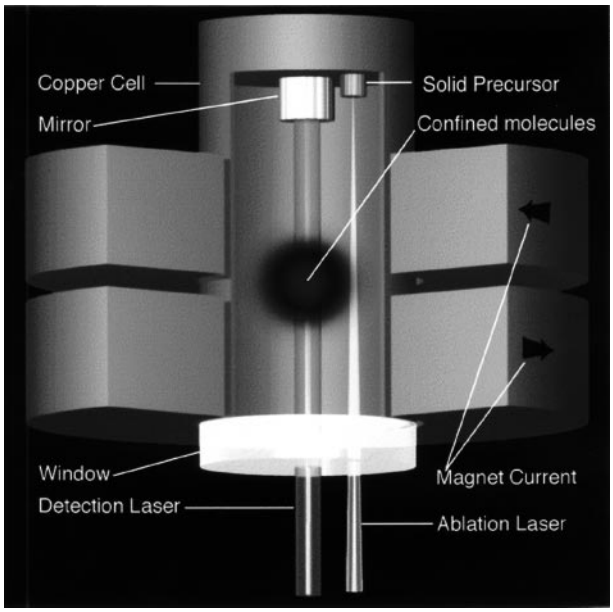

Fig. 4. Section through the core elements of the buffer-gas loaded magnetic trap. Vacuum isolates the relatively warm (4 K) magnet from the cell whose temperature can be varied between 100 and 800 mK using a resistive heater. The magnet coils are arranged in the anti-Helmholtz configuration (currents travel in opposite directions) and form a magnetic trap up to 3 T deep. The fused silica window at the bottom of the cell enables entry of the detection and ablation lasers and extraction of the probe beam and the fluorescence.

a tube of 5 cm diameter and 0.8 mm wall thickness. The cell (inner/outer diameter of 4.27/4.50 cm and length of 6.8 cm) is made of OFE copper with a 4.4 cm diameter fused silica window sealing the bottom. On the inner top surface there is a 1 cm diameter mirror. A solid lump of the precursor material (the source of the atoms or molecules) is positioned near the mirror. The top of the cell is thermally anchored to the mixing chamber of the dilution refrigerator *via* a copper rod of 1.3 cm diameter. The temperature of the cell can easily be varied from 100 mK to 800 mK using a resistive heater. A section through the core elements of the apparatus is shown in Figure 4.

Our detection method is either absorption spectroscopy (used mainly for atoms but also with molecules) or laser induced fluorescence (used only for molecules). Figures 5 and 6 show the respective setups. A probe beam is generated by an actively stabilized ring laser (Coherent 899-21) used either in the Ti:sapphire or dye configuration. The typical power used to probe the atoms is 0.1 μW and up to 10^4 fold to excite the fluorescence of molecules. The probe beam enters at an angle with respect to the cell axis and passes through the cell center with a small offset. The beam then reflects from the mirror at the top of the cell, passes the cell center again, exits the cell, and is detected by a photo-multiplier tube. The fluorescence is reflected into a photomultiplier tube or a CCD camera preceded by a set of filters that suppress the probe beam scatter. The details of the techniques used to detect the individual trapped species are given below.

A pulsed doubled YAG laser beam (Continuum I-10, 532 nm, 5 ns pulse width, 15 mJ typical pulse energy) is used to ablate the solid precursor material.

2.3 Procedure

Our trapping procedure begins with the cryogenic cell filled either with ^{4}He or ^{3}He gas. Two types of loading were used [9].

In the first, designated as *normal loading*, the temperature of the cell is raised prior to ablation. The cell is heated to a temperature corresponding to the desired density ($\sim 10^{16}$ cm^{-3}) of the helium buffer gas. Then the ablation laser is fired, producing atoms and molecules that diffuse through the buffer gas and thermalize with it. After ablation, the cell temperature is lowered. This cryopumps the helium gas to the walls of the cell.

In the second method, termed *cold loading*, the cell is not heated prior to ablation. The cell is cold ($\sim$ 100 mK) and, therefore, a negligible amount of helium is in the gas phase before the ablation laser is fired; it is condensed as a liquid on the interior of the cell. Nevertheless, the trap can still be successfully loaded. We believe cold loading works because the ablation pulse brings into the gas phase not only the species-to-be-trapped, but simultaneously evaporates the condensed helium that subsequently quickly thermalizes. After the pulse, buffer-gas loading proceeds as usual. The advantage of cold loading is a faster cooling of the cell, as its temperature drops from a lower initial value. If we infer the helium pressure from the cell temperature [5], then within 5 s of the ablation pulse the background pressure of ^{3}He and ^{4}He is less than 10^{-7} and 10^{-18} torr, respectively.

3 Trapping of atomic chromium

Chromium is ideally suited for magnetic trapping experiments: it has a large magnetic dipole moment of $6\mu_B$ (Bohr magneton) and occurs in four isotopes, three of which are bosons and one is a fermion. Chromium trapping can thus lead to the study of Bose-Einstein condensates [10] as well as of a Fermi degenerate gas [11–14]. Chromium trapping may also benefit atom lithography research [15,16].

3.1 Experiment

The cell is filled either with ^{3}He or ^{4}He buffer gas. A sufficient amount of ^{3}He (^{4}He) is present so that at temperatures above 0.3 K (0.9 K) the density is approximately 10^{17} cm^{-3}. Below these temperatures, the density is determined by the helium vapor pressure. The Cr atoms are brought into the gas phase by single-pulse laser ablation of a solid sample of isotopically pure ^{52}Cr. The solid ^{52}Cr is positioned at the edge of the trapping region inside the cell. The atoms are detected by laser absorption spectroscopy on the $a^7S_3 \leftrightarrow z^7P_3$ transition at 427.6 nm [17,18]. The probe beam is produced by doubling the output of a continuous wave Ti:sapphire laser with a $KNbO_3$

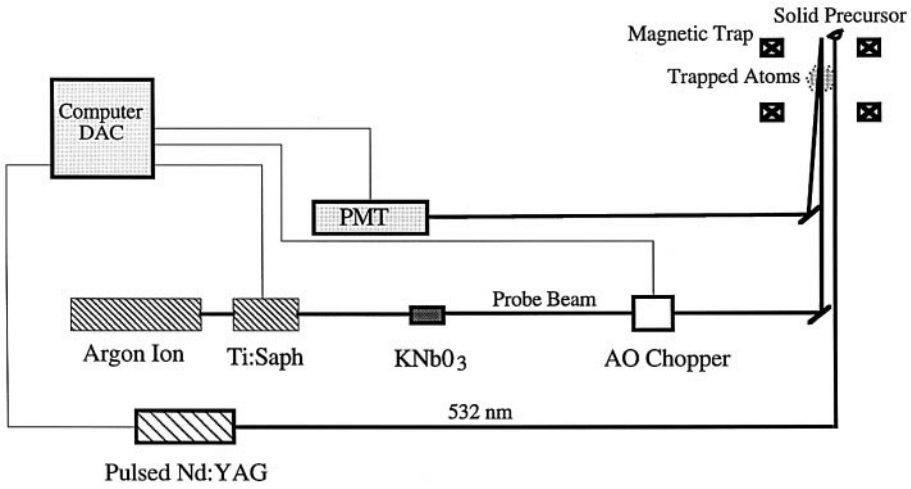

Fig. 5. Experimental setup used for the detection of the trapped sample by absorption spectroscopy.

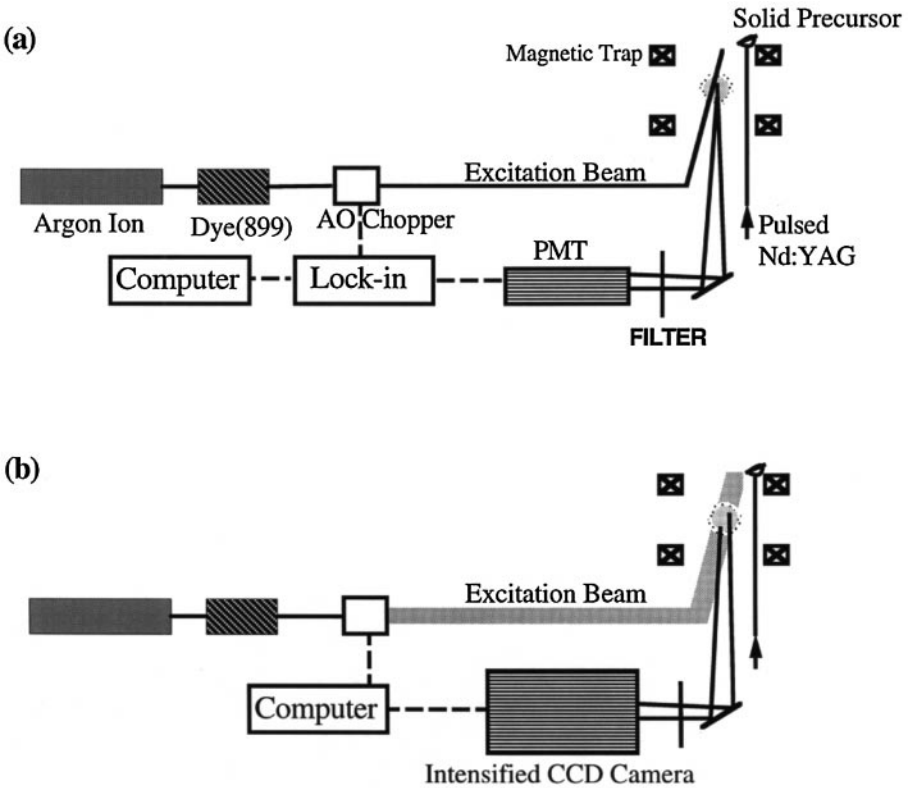

Fig. 6. Experimental setup used for the detection of the trapped sample by fluorescence spectroscopy using a photomultiplier tube (a) or a CCD camera (b).

crystal. Typical probe power used is $\sim 10^{-7}$ watt. With the above apparatus, we were able to produce, thermalize, and trap neutral, ground-state ^{52}Cr atoms. Both normal and cold loading methods were used.

3.2 Results

Shown in Figure 7 are spectra of the trapped chromium taken 2 s after ablation, using ^{4}He as the buffer gas and a trap depth of 2.4 T. Also shown are simulations of the spectra. These are based on theory presented in the Appendix (low-field limit). In calculating the spectra we assumed a thermal distribution of atoms within our trap. The $M_J = 3$ ($6\mu_B$) state of ^{52}Cr is trapped. The number density of atoms within our trap was obtained from these spectral simulations. In the case of cold loading, the temperature was determined from this fit as well. With normal loading, we were able to load in 1×10^{11} chromium atoms into our trap, with a peak density of 5×10^{11}

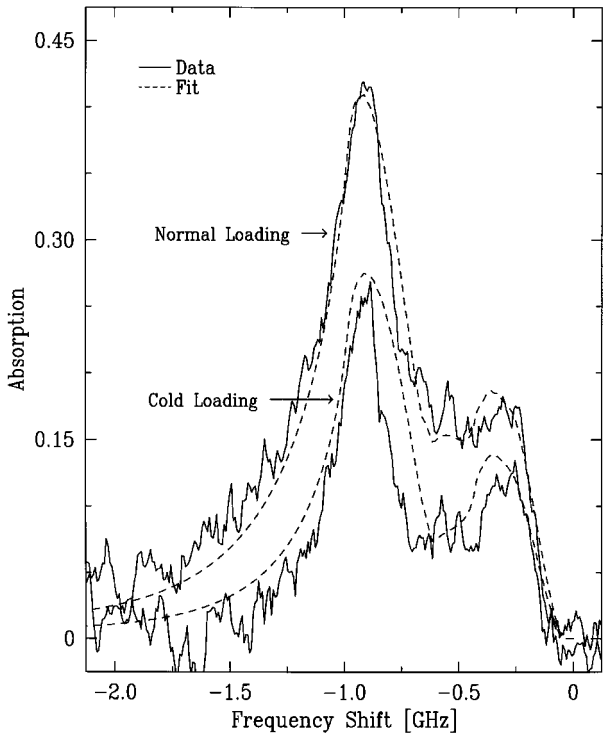

Fig. 7. Absorption spectra of trapped ^{52}Cr(a^7S_3) obtained by scanning over 4 GHz in 100 ms about the center frequency of the $a^7S_3 \leftrightarrow z^7P_3$ transition at 23.386 cm^{-1} (427.6 nm). Spectra taken 2 s after the ablation pulse. Broadening is primarily due to Zeeman shifts. The double peaked structure is due to the probe beam passing through the cloud of trapped chromium atoms twice, at two different distances from the trap center. The frequency zero is the location of the field-free line center.

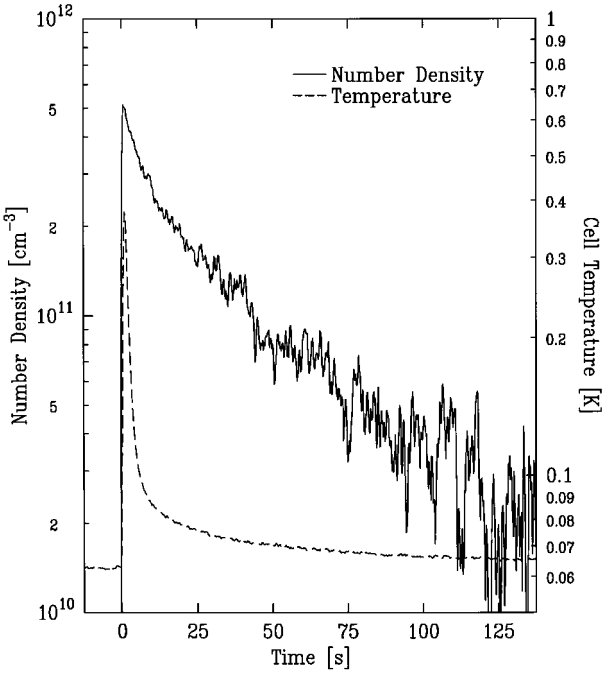

Fig. 8. Time profile of the absorption signal due to Cr atoms trapped *via* ^{4}He cold loading in a 2.4 T trap. Measurement of the cell temperature is limited by the slow time response of the resistive thermometer; as a result, readings up to 3 s are of limited accuracy.

at a temperature of 1 K. With cold loading, slightly fewer atoms were trapped: 2 s after loading, 4×10^{10} atoms at a density of 4×10^{11} were trapped. Quoted atom numbers and densities are accurate to within a factor of 2. No significant attempt was made to increase the number of trapped atoms by optimizing the loading procedure.

The decay of the trapped chromium is shown in Figure 8. By 20 s after the ablation pulse the temperature had returned to a low-enough value so that most of the He buffer gas had been cryopumped to the cell walls. The time profile was obtained by monitoring the Cr absorption at a fixed frequency corresponding to the maximum absorbance in Figure 7. The number density was calculated from this absorption and a spectrum taken at a short delay time. If we fit the decay to purely one-body loss (exponential decay, $\dot{n} = -n/\tau$) we find a time constant $\tau = 44$ s. If we fit to a purely two-body loss, ($\dot{n} = -Gn^2$) we find $G = 2 \times 10^{-12}$ cm^{-3} s^{-1}. Fitting to a combined one- and two-body loss ($\dot{n} = -n/\tau - Gn^2$) yields $\tau = 76$ s and $G = 7 \times 10^{-13}$ cm^{-3} s^{-1}.

While the pure one-body fit is better than the pure two-body fit, it is not clear what could be causing one-body decay in our sample. Suspect mechanisms are evaporation of atoms over the trap edge, Majorana transitions at the low-field trap center, and optical pumping by the probe beam. However, our sample is at a sufficiently high η (≈ 13) that evaporative losses should be negligible. Our trap parameters are such that Majorana losses would take place on a much longer timescale [8,19]. Optical pumping seems unlikely, as the probe power was varied over a wide range with little effect on the timescale of the absorption signal.

One possible explanation of the apparent one-body loss in our trap is inaccuracy in our calculation of the chromium density. We compute the density at a given time from the absorption at a single frequency at that time and a spectrum of the atoms taken at a fixed time. It is assumed that the distribution of atoms is not changing over the trap lifetime. However, if the distribution (and hence the spectrum) changes over time due to cooling or heating in the trap, this would distort the calculation. This could make the fitting process inconclusive as to the exact nature of our loss.

We also loaded ^{52}Cr into our trap using ^{3}He as a buffer gas. The advantage of loading with ^{3}He is that its higher vapor pressure allows buffer gas loading at lower temperatures than does ^{4}He and thus at higher η. With ^{3}He buffer gas and normal loading, we loaded 5×10^{11} Cr atoms at a temperature of 300 mK into a magnetic trap of depth 0.7 tesla.

The $6\mu_B$ magnetic moment of Cr allows loading of our trap at elevated temperatures. With the cell at 1.4 K, we were able to load $\sim 10^{11}$ Cr atoms. This is of interest because temperatures of 1.3 K can be easily reached

with a pumped ^{4}He cryostat. Such a cryostat is comparably simpler than the dilution refrigerator system we currently use. Cr and other large-magnetic moment atoms could be trapped using this simple cryostat. Although a pumped ^{4}He refrigerator cannot reach the cold temperatures necessary to lower the vapor pressure of liquid helium, it should be possible to remove the helium buffer gas from the cell by cryopumping it with charcoal [20].

4 Trapping of atomic europium

Our choice of ground state Eu atoms ($^8S_{7/2}, g = 1.993$) as a test species (the first that we trapped) was led in part by considerations of principle and in part of experimental convenience: the large paramagnetism of Eu makes it easy to trap and the high oscillator strength of its visible transitions makes it easy to detect [21]. The nuclear spin, $I = 5/2$, of both of its naturally occurring isotopes, ^{151,153}Eu, presented an opportunity to test the hyperfine spectroscopy of a trapped atom and to learn about the relaxation dynamics of the hyperfine states.

4.1 Experiment

We first investigated the thermalization of laser ablated Eu as a function of He temperature, ranging between 300 K and 250 mK. In this preparatory work the Eu atoms were detected by absorption spectroscopy within the (red) $z^{10}P_{7/2} - a^8S_{7/2}$ band (4 μs lifetime, 710.8 nm) [22]. The Eu temperature was measured using the Doppler width of the hyperfine lines. With 4 μmole of ^{3}He (loaded into the 95 cm^3 cell), the ablated atoms were found to thermalize with the He gas on a time scale of 1 ms at 77 K, 4 ms at 4 K, and 30 ms at 250 mK. These times are consistent with a simple model of thermalization using a He-Eu elastic collision cross-section of 10^{-14} cm^2 at 4 K.

The trap is typically loaded using ^{4}He as buffer gas and with a magnetic trap depth of $\mathcal{H}_{\rm edge} = 2$ T ($\mathcal{H}_{\rm edge} = 0.6$ T with ^{3}He buffer gas). Normal loading was used, *i.e.* the trapping procedure began by raising the cell temperature to 800 mK (250 mK with ^{3}He). Then a single YAG pulse ablates the lump of europium and the heater is simultaneously turned off. The temperature of the cell rises for about 1 s due to heating by the YAG pulse but then quickly decreases. Over the course of 20 s the temperature of the cell and the He can drops to 230 mK (170 mK with ^{3}He) where the ^{4}He density is about 1×10^4 cm^{-3} (4×10^{13} cm^{-3} with ^{3}He) [5,6]. These densities correspond to room temperature pressures of 3×10^{-13} torr (1.3×10^{-3} torr for ^{3}He). The trapped atoms are then probed with the blue beam tuned to the $y^8P_{7/2} - a^8S_{7/2}$ band (6 ns lifetime, 462.7 nm) [22,23].

Data is taken in one of two ways: either absorption time profiles at given wavelengths are measured or the laser is scanned over the entire absorption band of about 13 GHz at certain fixed delay times after the ablation pulse. The absorption spectrum can be measured many times for each trapped sample (scan time much shorter than the trapping time, see below), yielding good signal to background ratios.

4.2 Theory

Although the theory of atomic hyperfine spectra is straightforward, all its ingredients are seldom presented in one place; therefore, we give a brief recapitulation below.

The Hamiltonian of an atom with total electronic angular momentum $\mathbf{J}$ and nuclear spin $\mathbf{I}$ subject to a magnetic field $\mathcal{H}$ takes the form [24]:

$$H = g_{\rm J}\mu_{\rm B}\mathbf{J}\cdot\mathcal{H} + g_{\rm I}\mu_{\rm B}\mathbf{I}\cdot\mathcal{H} + a\mathbf{I}\cdot\mathbf{J} + b\frac{(3/2)\mathbf{I}\cdot\mathbf{J}(2\mathbf{I}\cdot\mathbf{J}+1) - \mathbf{I}^2\cdot\mathbf{J}^2}{2I(2I-1)J(2J-1)} \quad (10)$$

where J and I are the electronic and nuclear angular momentum quantum numbers, $g_{\rm J}$ and $g_{\rm I}$ the corresponding g-factors, a and b the hyperfine magnetic dipole and electric quadrupole coupling constants, and $\mu_{\rm B}$ the Bohr magneton. The matrix elements of H can be obtained analytically either in the coupled basis, $|F, M\rangle$, corresponding to the weak-field limit or in the uncoupled basis, $|M_J, M_{\rm I}\rangle$, corresponding to the strong-field limit. Hence either yields the eigenenergies and line strengths in closed form.

4.2.1 Low-field limit

In the low-field limit, the angular momenta $\mathbf{J}$ and $\mathbf{I}$ couple to a resultant total angular momentum $\mathbf{F} = \mathbf{J} + \mathbf{I}$ characterized by a quantum number $F = J + I, J + I - 1, ..., |J - I|$; each value of F has $2F + 1$ projections $M = -F, -F + 1, ..., +F$ on the space-fixed axis defined by the direction of $\mathcal{H}$. Note that there are $\sum_F(2F+1) = (2J+1)(2I+1)$ coupled states $|F, M\rangle$. The eigenenergy is given by

$$E(F,M) = \frac{1}{2}aK + b\frac{(3/4)K(K+1) - I(I+1)J(J+1)}{2I(2I-1)J(2J-1)} + Mg_{\rm F}\mu_{\rm B}\mathcal{H} \quad (11)$$

where

$$K \equiv F(F+1) - J(J+1) - I(I+1) \quad (12)$$

and

$$g_{\rm F} = g_{\rm J}\frac{F(F+1) + J(J+1) - I(I+1)}{2F(F+1)} \quad (13)$$

with $g_{\rm J}$ given by equation (A.3). The line strength factor $S_q(IJ'F'M'; IJFM)$ of a transition between states $|IJ'F'M'\rangle \leftarrow |IJFM\rangle$ due to an electric dipole moment d_q (of unit magnitude, with $q = 0$ for parallel and $q = \pm 1$ for perpendicular transitions) is given by

$$S_q = |\langle IJ'F'M'|d_q|IJFM\rangle|^2 \quad (14)$$

with

$$\langle IJFM|d_q|IJ'F'M'\rangle = (-1)^{F-M'+J'+I+F+1}[(2F+1)(2F'+1)]^{1/2} \times \begin{pmatrix} F & 1 & F' \\ -M & q & M' \end{pmatrix} \begin{Bmatrix} J & 1 & F \\ F' & I & J \end{Bmatrix} \langle J||d||J'\rangle. \quad (15)$$

4.2.2 Strong-field limit

In the strong-field limit, the angular momenta **J** and **I** are no longer integrals of motion but their projections M_J and M_I on the space-fixed axis are. Since M_J and M_I take respectively $(2J+1)$ and $(2I+1)$ values, there are $(2J+1)(2I+1)$ uncoupled states $|M_\mathrm{J}, M_\mathrm{I}\rangle$. In the uncoupled basis, the eigenvalues of Hamiltonian (10) are given by

$$E(M_\mathrm{J}, M_\mathrm{I}) = M_\mathrm{J} g_\mathrm{J} \mu_\mathrm{B} \mathcal{H} + M_\mathrm{I} g_\mathrm{I} \mu_\mathrm{B} \mathcal{H} + a M_\mathrm{J} M_\mathrm{I} + \frac{9b}{4I(2I-1)J(2J-1)} \left[M_\mathrm{J}^2 - \frac{1}{3}J(J+1)\right] \times \left[M_\mathrm{I}^2 - \frac{1}{3}I(I+1)\right] \quad (16)$$

(neglecting the magnetic octupole and higher-order interactions).

The line strength factor $S_q(M'_\mathrm{J}, M'_\mathrm{I}; M_\mathrm{J}, M_\mathrm{I})$ of a transition between states $|M'_\mathrm{J}, M'_\mathrm{I}\rangle \leftarrow |M_\mathrm{J}, M_\mathrm{I}\rangle$ due to an electric dipole moment d_q (of unit magnitude, with $q = 0$ for parallel and $q = \pm 1$ for perpendicular transitions) is given by

$$S_q = |\langle M'_\mathrm{J}, M'_\mathrm{I}|d_q|M_\mathrm{J}, M_\mathrm{I}\rangle|^2 \quad (17)$$

with

$$\langle M'_\mathrm{J}, M'_\mathrm{I}|d_q|M_\mathrm{J}, M_\mathrm{I}\rangle = (-1)^{J-M_\mathrm{J}} \delta(M'_\mathrm{I}, M_\mathrm{I}) \begin{pmatrix} J & 1 & J' \\ -M_\mathrm{J} & q & M'_\mathrm{J} \end{pmatrix} \langle J||d||J'\rangle. \quad (18)$$

4.2.3 Populations and intensities

The initial field-free populations, $P(F)$, of an F-state at a temperature T are given by

$$P(F) = (2F+1)\exp\left(-\frac{E_\mathrm{F}}{kT}\right). \quad (19)$$

Due to the small spacing of the hyperfine energy levels, the Boltzmann factor $\exp(-E_\mathrm{F}/kT) \to 1$ and the initial field-free populations are in general determined essentially by the degeneracy factor, $P(F) \to (2F+1)$. In keeping with this, the initial populations in the low-field limit are equal, *i.e.* each $|F, M\rangle$ state has the same weight. If the atoms were created in low field and thermalization of hyperfine states did not occur, then in the high-field limit the initial

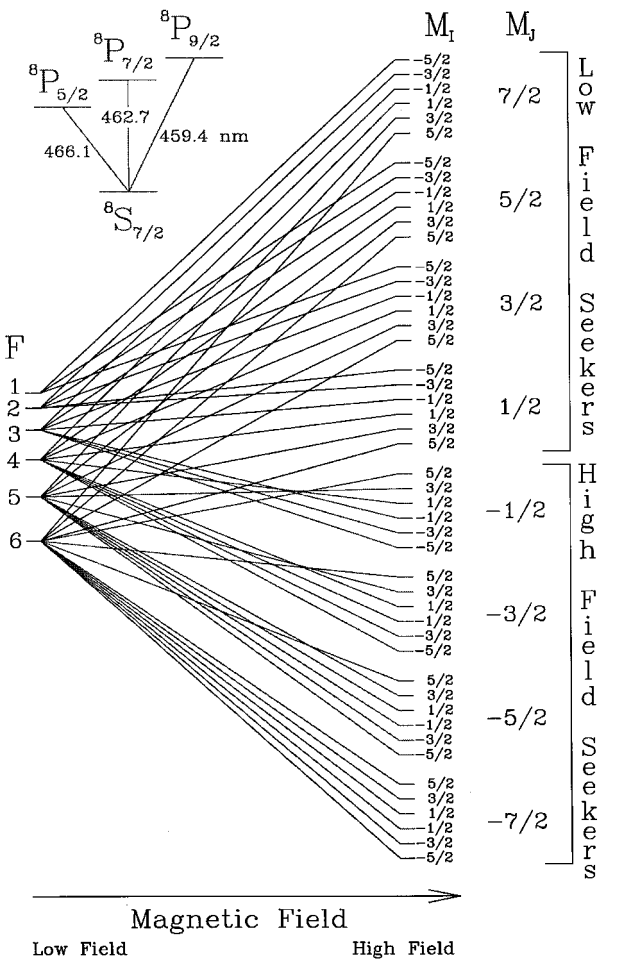

Fig. 9. Correlation diagram between the low- and high-field limits for the states of either of the stable isotopes of Eu($a^8\mathrm{S}_{7/2}$). Also shown is the transition to the $y^8\mathrm{P}_{7/2}$ state used to probe the atoms.

populations of the $|M_\mathrm{J}, M_\mathrm{I}\rangle$ states are determined by adiabatic transfer of the low-field populations of the $|F, M\rangle$ states which, in turn, is given by the transformation of the coupled to the uncoupled basis:

$$P(M_\mathrm{J}, M_\mathrm{I}) \propto \langle JM_\mathrm{J}, IM|FM\rangle^2 = (2F+1)\begin{pmatrix} J & I & F \\ M_\mathrm{J} & M_\mathrm{I} & -M \end{pmatrix}^2. \quad (20)$$

In our experiments, we create the atoms at high field and high temperature where, apparently, the hyperfine states are equally populated (see the simulations below). The correlation between the low- and high-field limits is determined by the non-vanishing 3-J symbols. The corresponding correlation diagram is shown in Figure 9.

The intensities, $\mathcal{I}$, of the transitions between states in absorption or excitation spectra are then given by

$$\mathcal{I}(M'_\mathrm{J}, M'_\mathrm{I}; M_\mathrm{J}, M_\mathrm{I}) \propto P(M_\mathrm{J}, M_\mathrm{I}) S(M'_\mathrm{J}, M'_\mathrm{I}; M_\mathrm{J}, M_\mathrm{I}). \quad (21)$$

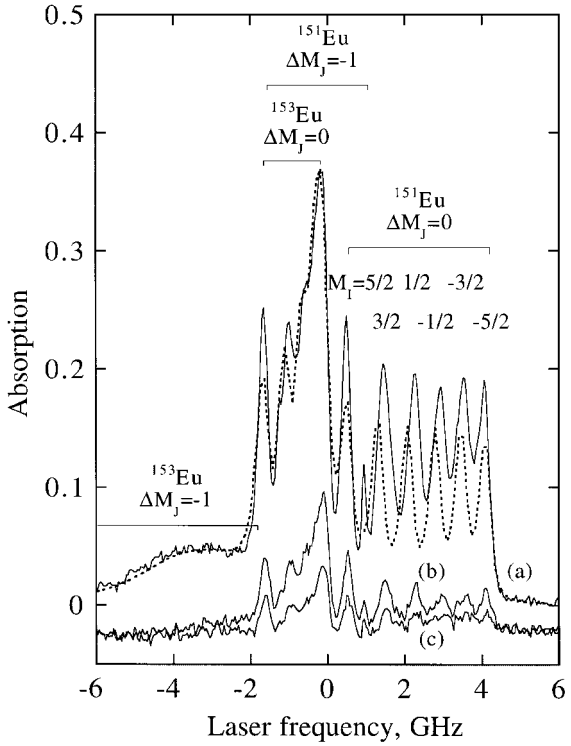

Fig. 10. Sample absorption spectra of the trapped ensemble of Eu at 0.6 T in the $a^8S_{7/2} \leftrightarrow y^8P_{7/2}$ band at 462.7 nm measured (a) 20 s, (b) 40 s, and (c) 60 s after the ablation pulse. For clarity, the (b) and (c) spectra are shifted on the absorbance scale by −0.025. The simulated spectrum, shown by the dotted line, provides the indicated assignment of the lines: all features are due to the $M_J = 7/2$ state of Eu($a^8S_{7/2}$). For each isotope, there are two sub-bands of magnetic hyperfine transitions, with $\Delta M_J = 0$ and −1. Note that for the $\Delta M_J = 0$ transitions in the ^{151}Eu isotope, all six M_I nuclear spin states are clearly resolved.

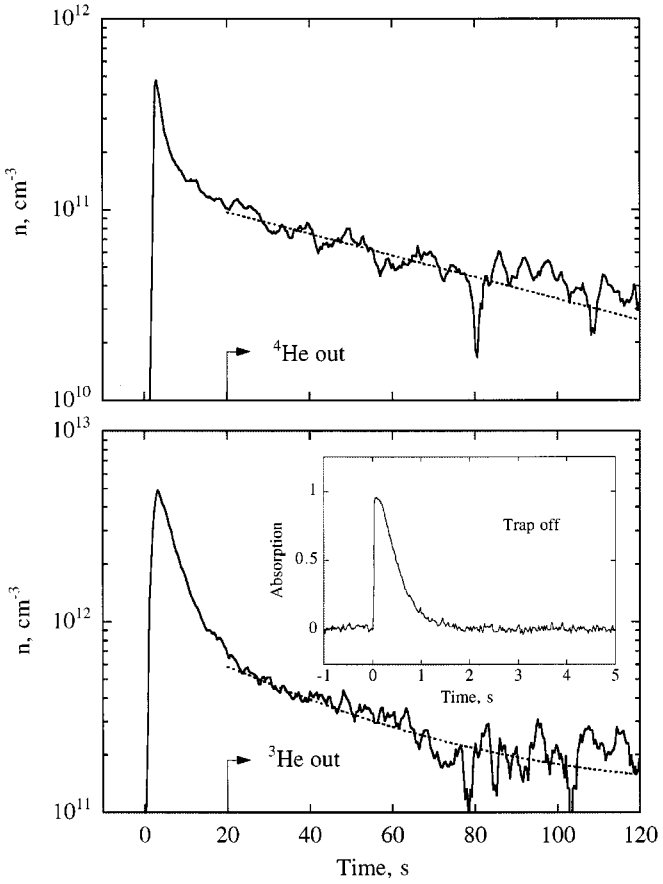

Fig. 11. Averaged absorption time profiles (full line) for ^{4}He at 800 mK (top) and ^{3}He at 250 mK (bottom) loading measured at a fixed frequency of the probe laser close to the band origin. A total of 4 (8) time profiles were averaged to obtain the displayed ^{4} He (^{3}He) data. Note that about 20 s after the ablation pulse (time zero) the density of the ^{4}He buffer gas drops to about 5×10^4 cm^{-3} (4×10^{13} cm^{-3} for ^{3}He). The data are fitted with a combined one-body and two-body loss rate function (dashed line). About 1×10^{12} atoms are initially loaded into the trap using ^{3}He buffer gas. The inset on the right shows an absorption time profile measured under the same conditions but with the trap off.

4.3 Results

Figure 10 shows sample spectra of the trapped ensemble at 0.6 T trap depth (250 mK loading temperature) measured 20, 40, and 60 s after the ablation pulse. One can see that the main features of the spectra change little with time but their integrated absorption intensities are proportionately decreasing.

The trap spectra were assigned on the basis of the spectral constants of ^{151,153}Eu taken from reference [23] and the distribution function of the number of atoms subject to a given $\mathcal{H}$-field, $N(\mathcal{H})$. The latter was determined for a given magnetic state and loading temperature from the calculated spatial distribution of the $\mathcal{H}$-field and factors accounting for the probe beam geometry.

From the simulations it follows that essentially only the $M_J = 7/2$ state is trapped. This corresponds well with our model of loading: the lower M_J states are not as tightly confined and leave the trap quickly. The corresponding simulated spectrum together with the assignment of the lines according to the isotope and hyperfine substrate is also shown in Figure 10. With this assignment, the initial temperature of the atoms in ^{3}He could be determined to be 250 ± 30 mK.

We also measured the absorption time profiles at fixed laser frequency and used the data to study the loss kinetics of the atoms from the trap. The absolute atom number was determined using the fitted values from the simulation of the spectra and the published line strength factors [25]. The atomic densities are a natural product of the same calculations. Our atom density and number is determined within ±60%. Figure 11 shows the time profile for ^{4}He and ^{3}He loading (upper and lower panel, respectively) assuming the atoms remain at the initial loading temperature. An initial density of 5×10^{12} cm^{-3} was achieved with ^{3}He loading.

The ^{4}He data (from 0 to 120 s) fits poorly to an exponential function (one-body loss). A combined Eu–Eu two-body loss and one-body loss yields good fits.

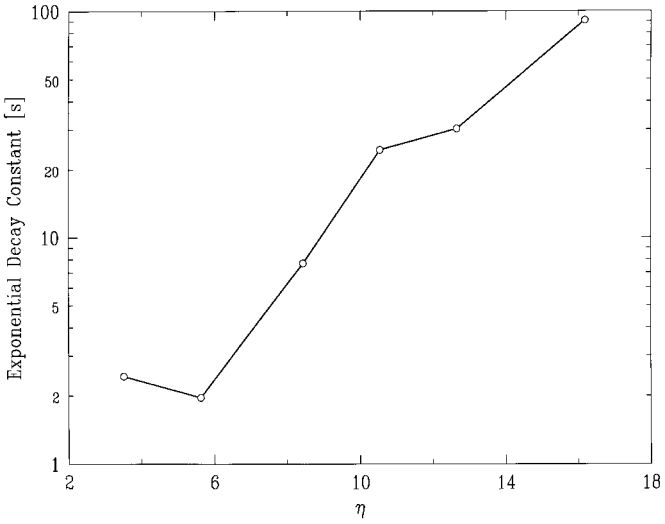

Fig. 12. Dependence of lifetime τ of trapped Eu on the trap depth parameter η. Data obtained at different buffer-gas temperatures and for different magnetic field strengths.

This combined fit is dominated by two-body loss and is shown as the smooth dashed line in the figure. Using only the data after the ^{4}He is pumped out (20–120 s) yields similar quality fits for either two-body or one-body loss. These fits result in a two-body collisional loss rate constant $G = 4 \pm 2.5 \times 10^{-14}$ cm^3 s^{-1} or an exponential time constant $\tau = 70 \pm 10$ s. However, after cryopumping ($t > 20$ s) the trapped sample is out of thermal contact with the cell walls and the temperature of the sample may change due to evaporative cooling. This uncertainty prevents rigorous interpretation of these loss rates.

The ^{3}He data also fits poorly assuming only a constant one-body loss but does fit well to two-body ($1/t$) loss. A combined one-body and two-body loss function was fitted to the data. From this and fits of similar data we determined the loss to be two-body with a two-body (Eu–Eu) collisional loss rate constant $G = 3 \pm 2 \times 10^{-14}$ cm^3 s^{-1} at a temperature of 170 mK. Unlike the ^{4}He case, here the sample *is* in thermal contact with the cell wall. Fits performed assuming a three-body process (Eu–Eu–Eu) yielded similar quality fits to the two-body fits. Thus, three-body loss cannot be ruled out, although it seems unlikely given the Eu densities present in the trap. Figure 12 shows the net lifetime of the Eu atoms in the trap as a function of the reduced trap depth η. This dependence is seen to be roughly exponential.

5 Trapping of calcium monohydride molecules

5.1 Experiment

The CaH molecules are created by ablating a solid sample of CaH_2 placed within the cell at the edge of the trapping region with a 10 mJ, 7 ns YAG pulse [26].

The CaH molecules are detected by laser fluorescence spectroscopy [26]. The fluorescence is excited at 635 nm in the $B^2\Sigma, v' = 0 \leftarrow X^2\Sigma, v'' = 0$ band [27,28] and detected mainly within the $B, v' = 0 \rightarrow X, v'' = 1$ band at 692 nm (the corresponding Franck-Condon factor was calculated to be 0.028, [29]). A set of color-glass and bandpass interference filters placed in front of the detector (either a photomultiplier tube or a CCD camera) serves to block the scattered probe radiation (along with the $B, v' = 0 \rightarrow X, v'' = 0$ fluorescence).

Typically, under field free conditions, only a single rotational transition, $N' = 1, J' = 3/2 \leftarrow N'' = 0, J'' = 1/2$, can be detected. This is consistent with a fast rotational relaxation of the molecules that renders the population of higher rotational states negligible: the next rotational state lies 8.5 cm^{-1}above the $N'' = 0, J'' = 1/2$ ground state and the intensity of the (unobserved) corresponding transition is well below 0.1% of the $N' = 1, J' = 3/2 \leftarrow N'' = 0, J'' = 1/2$ transition. This yields an upper limit on the rotational temperature of 1.5 K. Using absorption spectroscopy to calibrate the fluorescence detection, we found that up to 10^{10} CaH molecules could, under certain conditions, be formed by a single ablation pulse. We were also able to detect the formation of $X^2\Sigma, v'' = 1$ molecules, which were about 10–100 times fewer; their scarcity precluded them from being detected in the trap. However, we measured an upper limit of the $v'' = 1 \rightarrow v' = 0$ relaxation cross-section (in collisions with the ^{3}He buffer gas) to be 10^{-18} cm^2, which suggests that it should be possible to load them into the trap.

As the magnetic field is turned up, the field-free rotational transition is observed to split into two features shifted towards lower and higher frequencies. Below we give a theoretical analysis [31] that assigns the feature that shifts towards higher frequencies to the transition from the $N'' = 0, J'' = 1/2, M'' = 1/2$ low-field seeking state to the $N' = 1, J' = 3/2, M' = 3/2$ state, and the feature that shifts towards lower frequencies to the transition from the $N'' = 0, J'' = 1/2, M'' = -1/2$ high-field seeking state to the $N' = 1, J' = 3/2, M' = -3/2$ state.

Figures 13a and 13b display, respectively, spectra with negative and positive frequency shifts taken at different values of $\mathcal{H}_{\rm edge}$. All panels correspond to delay times of up to 25 ms (with respect to the ablation pulse) when molecules in both the low- and high-field seeking states are spread almost evenly over the cell and their distributions are nearly symmetric, peaked towards high field. This shape reflects the available phase space, which increases towards the edge of the trap due to the spherical geometry of the field and is further enhanced at the edge due to the saddle point.

At later times, the high-field seekers move towards the edge of the trap, hit the wall of the cell, stick to it, and are lost from the trap; the low-field seekers, on the other hand, move towards the center of the trap and by 300 ms their distribution is that of a trapped ensemble at $T = 400$ mK, close to the initial temperature of the buffer gas of 300 mK. This is displayed in Figure 14, which shows spectra taken at different time delays with respect to the ablation pulse. After about 300 ms the signal corresponding to the high-field seekers (left-hand peak) is absorbed by the noise,

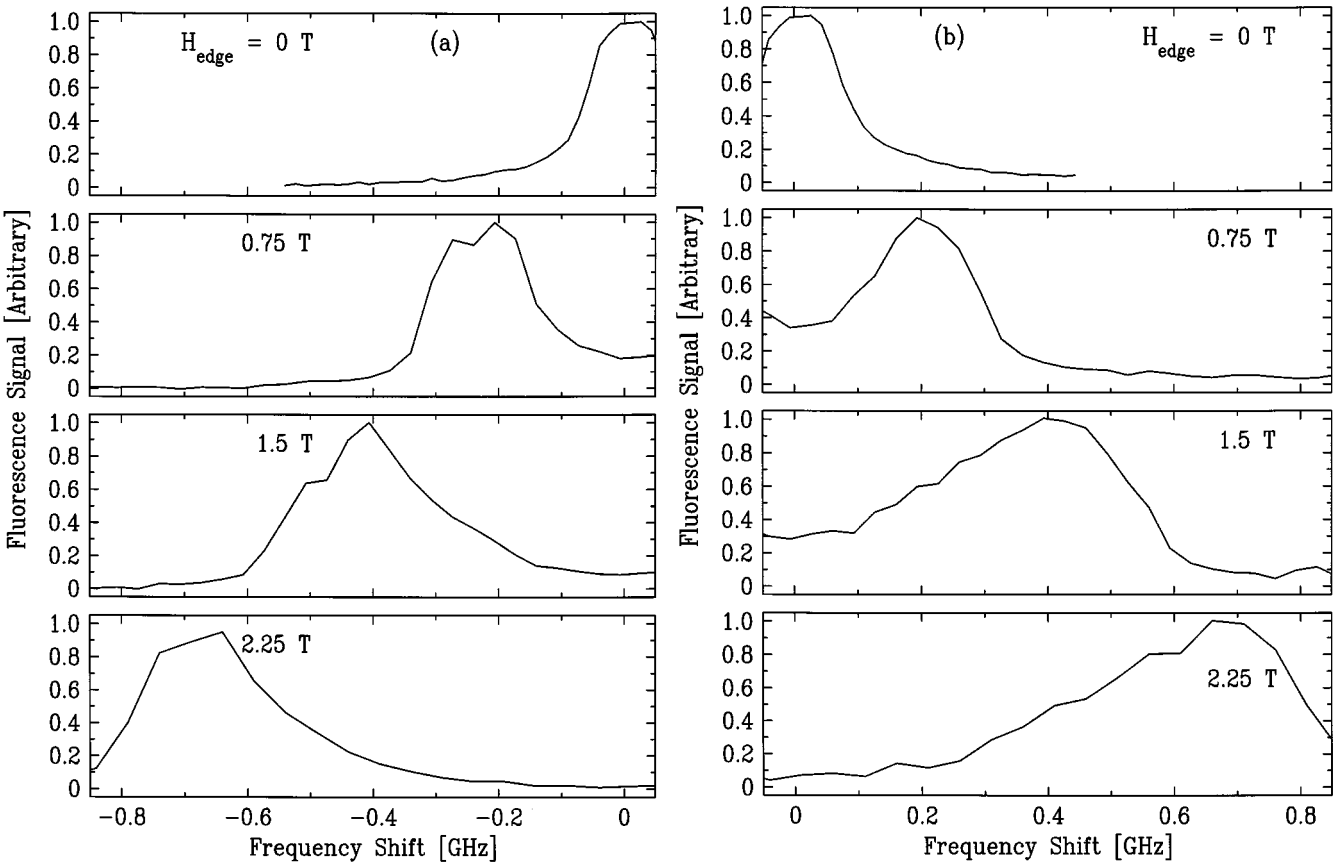

Fig. 13. Spectra taken at different values of the magnetic field at the edge of trap. All panels correspond to delay times of 25 ms with respect to the ablation pulse. The frequency scale is relative to the frequency of field-free transition $R_1(1/2)$. Part (a) shows spectra with a negative frequency shift corresponding to high-field seekers; part (b) shows spectra with positive frequency shift corresponding to low-field seekers. All spectra are normalized to the peak height.

see the lowest panel of Figure 14. Figure 15 shows this distribution together with a theoretical fit corresponding a temperature $T = 400$ mK and a number of molecules, $N = 10^8$. Figure 16 shows a CCD camera image of the trapped ensemble.

Figure 17 shows fluorescence time profiles of CaH integrated over negative and positive frequency shifts corresponding to high- and low-field seekers, respectively. About 1×10^8 molecules are initially loaded into the trap. The molecules have been observed to be trapped for more than 2 s with an exponential loss time constant $\tau = 0.6$ s. This behavior indicates evaporation of CaH molecules over the edge of the trap (where they stick to the walls) as the likely loss mechanism. Figure 18 shows the exponential dependence of the CaH lifetime in the trap on the depth.

We find that the slopes of the Zeeman curves for the $N' = 1, J' = 3/2, M' = \pm 3/2$ states differ from the slopes of the $N'' = 0, J'' = 1/2, M'' = \pm 1/2$ states (which are equal to $\pm g_S/2$ with g_S the electron spin gyromagnetic ratio) due to a perturbation of the $B^2\Sigma, v' = 0$ by a close-lying $A^2\Pi, v' = 1$ that lends the B state some of its A character (the perturbing rotational level of the A-state lies only 12.6 cm^{-1} above the $N' = 1, J' = 3/2$ level).

Figure 19 shows a correlation diagram between the low- and high-field limits for states from within the $X, v'' = 0$ and $B, v'' = 0$ manifolds; also shown are the perturbing states from within the $A, v' = 1$ manifold (dashed). The states from within the X and B manifolds are labeled by the Hund's case (b) angular momentum quantum numbers: N (rotation) and J (total, excluding nuclear spin) in the low-field limit and their projections on the direction of the field (the **Z** axis), M_N and M, in the high-field limit. The slopes of the eigenenergies in the high-field limit are determined by the projection, M_S, of the spin angular momentum on **Z** (the Paschen-Back uncoupling). The states involved in the spectroscopic transitions detected in our experiment are shown by bold lines. Note the different order of the eigenenergies (in J, N) in the X and B state manifolds in either limit – due to the opposite signs of the spin-rotation coupling constant [27,28]. While the field dependence of the states correlating with $N'' = 0$, $J'' = 1/2$ from within the X-state manifold is trivial, given by $\pm g_S \mathcal{H}/2$ for $M'' = \pm 1/2$, the Zeeman curves of the $N' = 1, J' = 3/2, M' = \pm 3/2, \pm 1/2$ states from within the $B^2\Sigma^+, v = 0$ state manifold are affected by a perturbation from the $A, v' = 1$ state. Their computation is the subject of the following section.

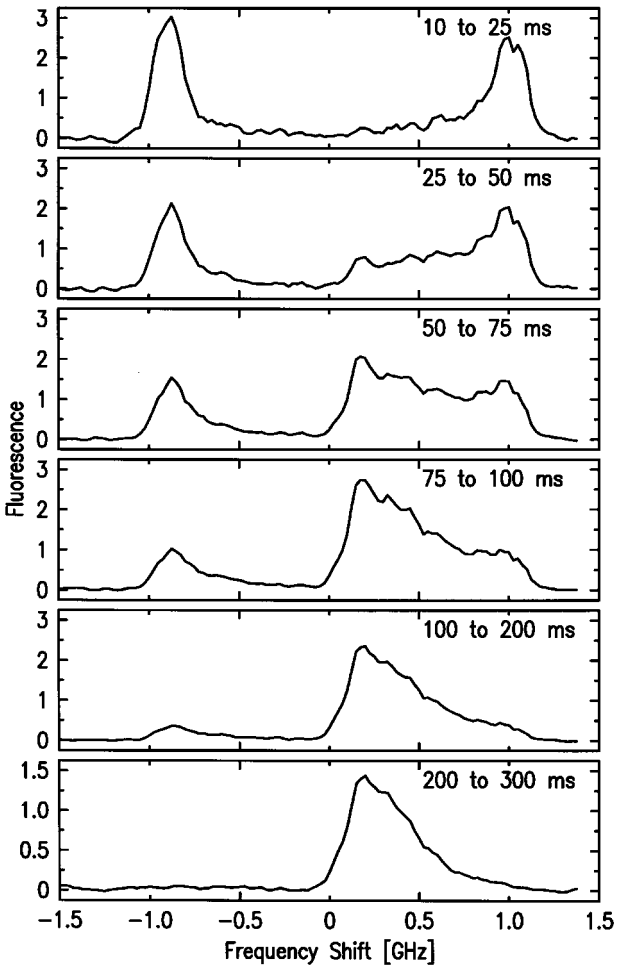

Fig. 14. Time evolution of the CaH spectrum. The data were obtained after firing a single ablation pulse and monitoring the fluorescence as a function of time at a single probe frequency. The process was repeated at different frequencies, and the fluorescence averaged over the specified time window in order to obtain the spectra. Times quoted are relative to the ablation pulse. The spectra reveal that high-field seekers (at negative frequency shifts) quickly leave the trap. The trapped low-field seekers (positive frequency shifts) are confined and compressed towards the center of the trap.

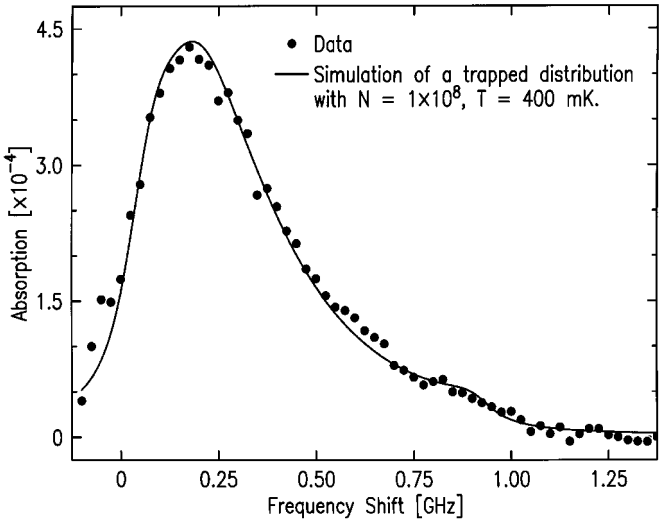

Fig. 15. Fit of CaH spectrum to a thermal distribution of trapped molecules. Data were taken with a 3 T trap depth and a cell temperature of 300 mK before ablation, and were integrated from 200 ms to 300 ms after the ablation pulse. This fit determines the number and the temperature of trapped CaH molecules to be $N = 1 \times 10^8$ and $T = 400$ mK.

5.2 Theory

5.2.1 Field-free rotational perturbations

In the absence of an external field, the Hamiltonian of a linear molecule is given by the sum of the vibronic, rotational, spin-spin, and spin-orbit Hamiltonians:

$$H_0 = H_{\rm ev} + H_{\rm r} + H_{\rm ss} + H_{\rm so} \tag{22}$$

In what follows we will consider the interaction of a $^2\Sigma, v_\Sigma$ with a $^2\Pi, v_\Pi$ vibronic state. For this case, Hamiltonian (22) simplifies since $H_{\rm ss} = 0$, as in any doublet state. Hence, the $^2\Sigma, v_\Sigma \sim {}^2\Pi, v_\Pi$ perturbation (described by the off-diagonal matrix elements of H_0) is due to the vibronic overlap and the L- and S-uncoupling and spin-orbit interactions.

In order for two rotational states to interact, their total angular momenta (excluding nuclear spin), $\mathbf{J}$, and their parities, $\mathbf{P}$, must be the same and the overlap of the vibrational eigenfunctions of the two states must be nonzero [32]. Therefore, to construct a suitable representation of the field-free Hamiltonian, we need a basis set of states with definite parity that correspond to the three electronic states in question: a $^2\Sigma$ state ($|\Omega| = 1/2$) and two $^2\Pi$ states (one with $|\Omega| = 1/2$ and one with $|\Omega| = 3/2$). Such a basis set, describing an intermediate coupling between Hund's cases (a) and (b), has been introduced by Radford and Broida [33]:

$$|1, c/d, J\rangle = (2)^{-1/2}\left({}^2\Sigma_{1/2} \pm {}^2\Sigma_{-1/2}\right) \tag{23}$$

$$|2, c/d, J\rangle = a\left({}^2\Pi_{3/2} \pm {}^2\Pi_{-3/2}\right) - b\left({}^2\Pi_{1/2} \pm {}^2\Pi_{-1/2}\right) \tag{24}$$

$$|3, c/d, J\rangle = b\left({}^2\Pi_{3/2} \pm {}^2\Pi_{-3/2}\right) + a\left({}^2\Pi_{1/2} \pm {}^2\Pi_{-1/2}\right) \tag{25}$$

where

$$a \equiv \left[\frac{X + (2-\lambda)}{4X}\right]^{1/2} \tag{26}$$

$$b \equiv \left[\frac{X - (2-\lambda)}{4X}\right]^{1/2} \tag{27}$$

$$\lambda \equiv \frac{A}{B_\Pi} \tag{28}$$

$$X \equiv \left[4\left(J + \frac{1}{2}\right)^2 + \lambda(\lambda - 4)\right]^{1/2} \tag{29}$$

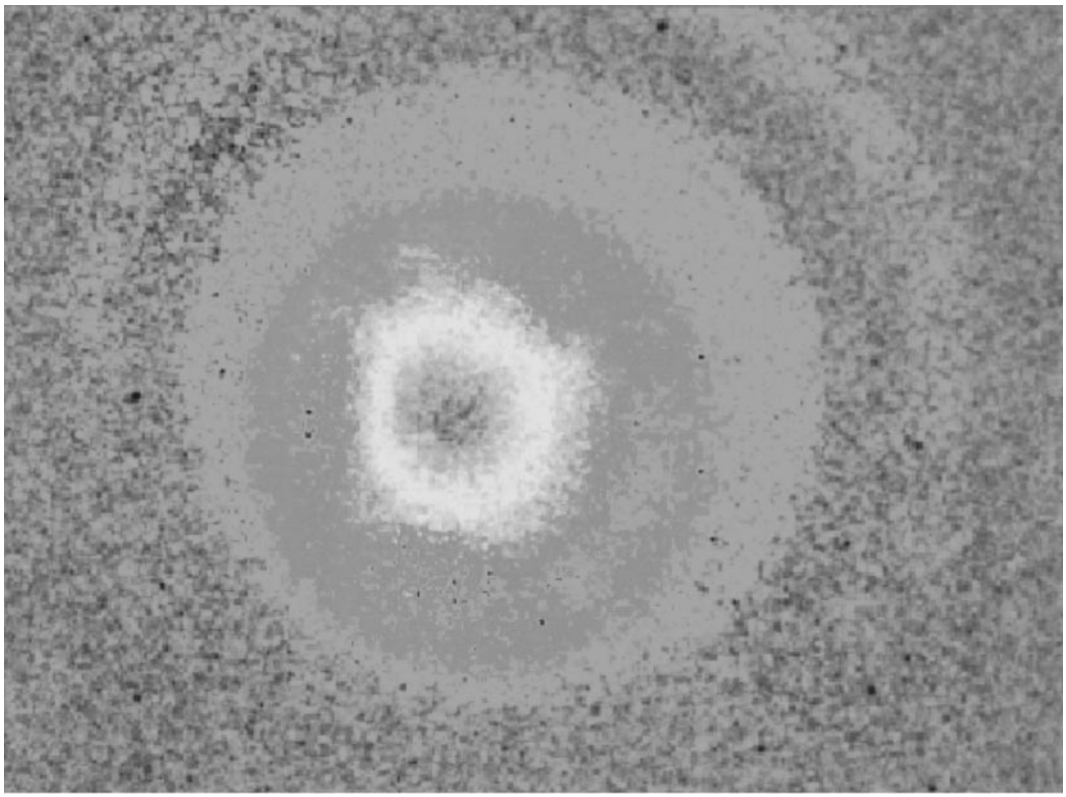

Fig. 16. A CCD camera image of the fluorescence due to a trapped CaH ensemble. Signal was integrated from 100 to 300 ms and from 0 to 1.1 GHz frequency shift.

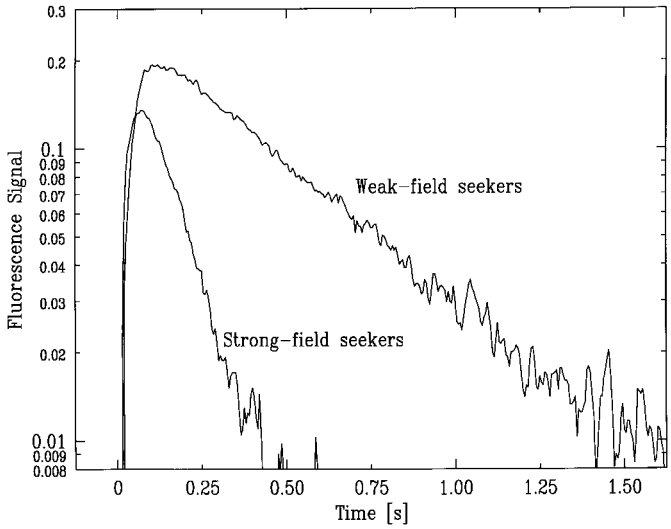

Fig. 17. Fluorescence time profiles (full line) for ^{3}He at 300 mK loading of CaH integrated over negative and positive frequency shifts corresponding to high- and low-field seekers, respectively. The data are fitted with a combined one-body and two-body loss rate function (dashed line). About 1×10^8 molecules are initially loaded into the trap.

and the upper and lower sign pertains respectively to the c and d symmetry. Note that $|1, c/d, J\rangle \rightarrow {}^2\Sigma_{|1/2|}$ and for $\lambda \rightarrow -\infty$, $|2, c/d, J\rangle \rightarrow {}^2\Pi_{|3/2|}$ and $|3, c/d, J\rangle \rightarrow {}^2\Pi_{|1/2|}$; for $\lambda \rightarrow \infty$, $|2, c/d, J\rangle \rightarrow {}^2\Pi_{|1/2|}$ and $|3, c/d, J\rangle \rightarrow {}^2\Pi_{|3/2|}$.

The matrix elements of the field-free Hamiltonian of a linear molecule in the Hund's case (a) basis that couple the ${}^2\Sigma$ and ${}^2\Pi$ states in question, first given by van Vleck [34], are [31]:

$$\langle {}^2\Sigma_{1/2} J|H_0|{}^2\Sigma_{1/2} J\rangle = \langle {}^2\Sigma_{-1/2} J|H_0|{}^2\Sigma_{-1/2} J\rangle = B_\Sigma \left[J(J+1) + \frac{1}{4}\right] + \Delta E \equiv \alpha \quad (30)$$

$$\langle {}^2\Pi_{1/2} J|H_0|{}^2\Pi_{1/2} J\rangle = \langle {}^2\Pi_{-1/2} J|H_0|{}^2\Pi_{-1/2} J\rangle = B_\Pi \left(J(J+1) + \frac{1}{4}\right) - \frac{A}{2} \equiv \beta \quad (31)$$

$$\langle {}^2\Pi_{3/2} J|H_0|{}^2\Pi_{3/2} J\rangle = \langle {}^2\Pi_{-3/2} J|H_0|{}^2\Pi_{-3/2} J\rangle = B_\Pi \left(J(J+1) - \frac{7}{4}\right) + \frac{A}{2} \equiv \gamma \quad (32)$$

$$\langle {}^2\Sigma_{1/2} J|H_0|{}^2\Sigma_{-1/2} J\rangle = \langle {}^2\Sigma_{-1/2} J|H_0|{}^2\Sigma_{1/2} J\rangle = B_\Sigma \left(J + \frac{1}{2}\right) \equiv (-1)^s \delta \quad (33)$$

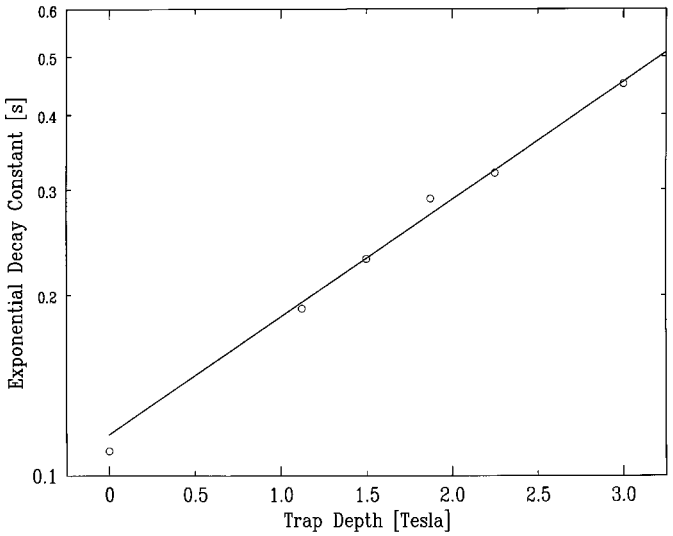

Fig. 18. Dependence of lifetime of trapped CaH on the trap depth parameter η. All data points were obtained for the same initial temperature of the ^{3}He-buffer gas of 300 mK.

$$\langle {}^2\Pi_{3/2} J|H_0|^2\Sigma_{1/2} J\rangle = \langle {}^2\Pi_{-3/2} J|H_0|^2\Sigma_{-1/2} J\rangle = B_\Pi \left[(J-\frac{1}{2})(J+\frac{3}{2})\right]^{1/2} \equiv \varepsilon \quad (34)$$

$$\langle {}^2\Pi_{1/2} J|H_0|^2\Sigma_{-1/2} J\rangle = (-1)^s \langle {}^2\Pi_{-1/2} J|H_0|^2\Sigma_{1/2} J\rangle = 2Q\left(J+\frac{1}{2}\right) \equiv (-1)^s \xi \quad (35)$$

$$\langle {}^2\Pi_{3/2} J|H_0|^2\Sigma_{1/2} J\rangle = (-1)^s \langle {}^2\Pi_{-3/2} J|H_0|^2\Sigma_{-1/2} J\rangle = 2Q\left[(J-\frac{1}{2})(J+\frac{3}{2})\right]^{1/2} \equiv \eta \quad (36)$$

$$\langle {}^2\Sigma_{1/2} J|H_0|^2\Pi_{1/2} J\rangle = (-1)^s \langle {}^2\Sigma_{-1/2} J|H_0|^2\Pi_{-1/2} J\rangle = P + 2Q \equiv \theta \quad (37)$$

with ΔE the energy difference between the zero-point energies of the Σ and Π states and

$$P \equiv \langle \Pi|\mathbf{AL}_y|\Sigma\rangle = \frac{1}{2}\langle \Pi|\mathbf{AL}^+|\Sigma\rangle \quad (38)$$

$$Q \equiv \langle \Pi|\mathbf{BL}_y|\Sigma\rangle = \frac{1}{2}\langle \Pi|\mathbf{BL}^+|\Sigma\rangle \quad (39)$$

the rotational perturbation parameters; $s = 0$ or 1 depending on whether the $\Lambda = 0$ state is Σ^+ or Σ^-. Using the matrix elements (30–37) we obtain for the matrix

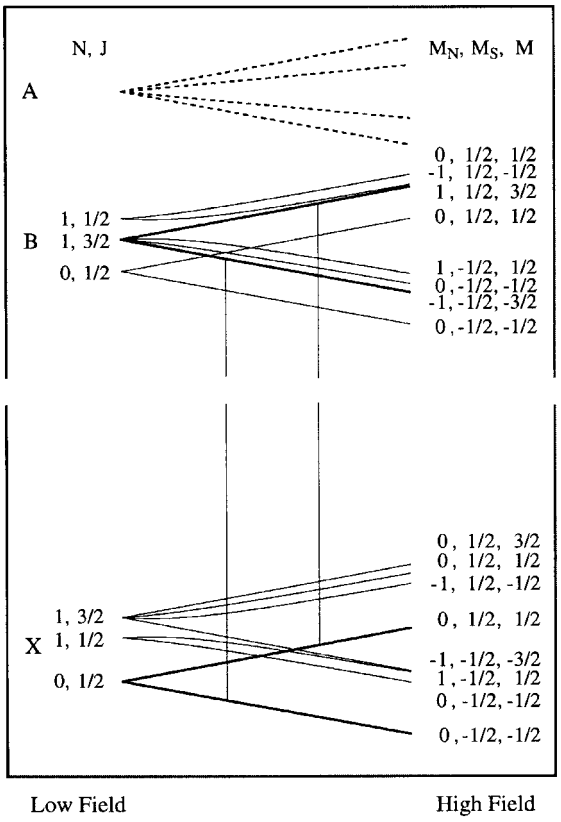

Fig. 19. A correlation diagram between the low- and high-field limits for states from within the $X, v'' = 0$ and $B, v'' = 0$ manifolds; also shown are the perturbing states from within the $A, v' = 1$ manifold (dashed). The states from within the X and B manifolds are labeled by the Hund's case (b) angular momentum quantum numbers: N (rotation) and J (total, excluding nuclear spin) in the low-field limit and their projections on the direction of the field (the **Z** axis), M_N and M, in the high-field limit. The slopes of the eigenenergies in the high-field limit are determined by the projection, M_S, of the spin angular momentum on **Z**. The states involved in the spectroscopic transitions detected in our experiment are shown by bold lines; the transitions are indicated by vertical lines.

elements of H_0 in the Broida-Radford basis [31]:

$$\langle 1, c/d, J|H_0|1, c/d, J\rangle = \alpha \pm \delta \quad (40)$$

$$\langle 2, c/d, J|H_0|2, c/d, J\rangle = 2(a^2\gamma - 2ab\varepsilon + b^2\beta) \quad (41)$$

$$\langle 3, c/d, J|H_0|3, c/d, J\rangle = 2(b^2\gamma + 2ab\varepsilon + a^2\beta) \quad (42)$$

$$\langle 1, c/d, J|H_0|2, c/d, J\rangle = 2^{1/2}[a\eta \mp b(\xi \pm \theta)] \quad (43)$$

$$\langle 1, c/d, J|H_0|3, c/d, J\rangle = 2^{1/2}[b\eta + a(\theta \pm \xi)] \quad (44)$$

$$\langle 2, c/d, J|H_0|3, c/d, J\rangle = 2[a^2\varepsilon + ab(\gamma - \beta) - b^2\varepsilon]. \quad (45)$$

In this formulation, the dependence of the eigenstates of H_0 on the electronic motion and the nuclear vibration is contained in the parameters $\xi = \xi(Q)$, $\eta = \eta(Q)$, and $\theta = \theta(Q, P)$ that depend on the perturbation parameters Q and P.

5.2.2 Rotational perturbation in the presence of an external magnetic field

The Hamiltonian of a molecule subject to a uniform magnetic field $\mathcal{H}$ is given by

$$H = H_0 + H_{\rm Z} \tag{46}$$

where the Zeeman Hamiltonian is [35]

$$H_{\rm Z} = -\boldsymbol{\mu}_{\rm Z}\mathcal{H} \tag{47}$$

with $\boldsymbol{\mu}_{\rm Z}$ the component of the molecular magnetic dipole moment operator along the space-fixed Z-axis whose direction is determined by $\mathcal{H}$. The magnetic dipole moment operator

$$\boldsymbol{\mu}_{\rm Z} = \frac{1}{2}(\Phi_{\rm Z}^{+}\mu^{-} + \Phi_{\rm Z}^{-}\mu^{+}) + \Phi_{\rm Z}^{z}\mu_z \tag{48}$$

depends on the body-fixed magnetic dipole moment operators

$$\boldsymbol{\mu}^{\pm} = -(g_{\rm L}\mathbf{L}^{\pm} + g_{\rm S}\mathbf{S}^{\pm})\mu_{\rm B} \tag{49}$$

$$\boldsymbol{\mu}_z = -(g_{\rm L}\mathbf{L}_z + g_{\rm S}\mathbf{S}_z)\mu_{\rm B} \tag{50}$$

(with $g_{\rm L} = 1$ and $g_{\rm S} \simeq 2.0023$ the orbital and spin gyromagnetic ratios and $\mu_{\rm B}$ the Bohr magneton) and the direction cosine operator Φ with components

$$\Phi_{\rm F}^{g} = \mathbf{F}\cdot\mathbf{g} \tag{51}$$

where $\mathbf{F} \equiv \mathbf{X}, \mathbf{Y}, \mathbf{Z}$ and $\mathbf{g} \equiv \mathbf{x}, \mathbf{y}, \mathbf{z}$ are unit vectors defining right-handed Cartesian space- and body-fixed coordinate systems. As a result,

$$\begin{aligned} H_{\rm Z} &= \left[\frac{1}{2}\left(\Phi_{\rm Z}^{+}\mathbf{L}^{-} + \Phi_{\rm Z}^{-}\mathbf{L}^{+}\right) + \Phi_{\rm Z}^{z}\mathbf{L}_z\right]\mu_{\rm B}\mathcal{H} \\ &\quad + \left[\frac{1}{2}\left(\Phi_{\rm Z}^{+}\mathbf{S}^{-} + \Phi_{\rm Z}^{-}\mathbf{S}^{+}\right) + \Phi_{\rm Z}^{z}\mathbf{S}_z\right] g_{\rm S}\mu_{\rm B}\mathcal{H} \\ &= (\mathbf{L}_{\rm Z} + g_{\rm S}\mathbf{S}_{\rm Z})\mu_{\rm B}\mathcal{H}. \end{aligned} \tag{52}$$

The Hund's case (a) matrix elements of $\mathbf{L}$ and $\mathbf{S}$ in the body-fixed, non-rotating frame for the states of interest are [30,31,35]

$$\langle {}^2\Sigma_{\pm1/2}|\mathbf{S}_z|{}^2\Sigma_{\pm1/2}\rangle = \pm\frac{1}{2} \tag{53}$$

$$\begin{aligned} \langle {}^2\Sigma_{\pm1/2}|\mathbf{S}^{\pm}|{}^2\Sigma_{\mp1/2}\rangle &= \langle {}^2\Pi_{1/2}|\mathbf{S}^{-}|{}^2\Pi_{3/2}\rangle \\ &= \langle {}^2\Pi_{3/2}|\mathbf{S}^{+}|{}^2\Pi_{1/2}\rangle \\ &= \langle {}^2\Pi_{-1/2}|\mathbf{S}^{+}|{}^2\Pi_{-3/2}\rangle \\ &= \langle {}^2\Pi_{-3/2}|\mathbf{S}^{-}|{}^2\Pi_{-1/2}\rangle = 1 \end{aligned} \tag{54}$$

$$\langle {}^2\Pi_{\pm1/2}|\mathbf{S}_z|{}^2\Pi_{\pm1/2}\rangle = \mp\frac{1}{2} \tag{55}$$

$$\langle {}^2\Pi_{\pm3/2}||\mathbf{S}_z|{}^2\Pi_{\pm3/2}\rangle = \pm\frac{1}{2} \tag{56}$$

$$\langle {}^2\Pi_{\pm1/2}|\mathbf{L}_z|{}^2\Pi_{\pm1/2}\rangle = \langle {}^2\Pi_{\pm3/2}||\mathbf{L}_z|{}^2\Pi_{\pm3/2}\rangle = \pm1 \tag{57}$$

$$\begin{aligned} \langle {}^2\Sigma_{\pm1/2}|\mathbf{L}^{\pm}|{}^2\Pi_{\mp1/2}\rangle &= \langle {}^2\Sigma_{1/2}|\mathbf{L}^{-}|{}^2\Pi_{3/2}\rangle \\ &= \langle {}^2\Pi_{3/2}|\mathbf{L}^{+}|{}^2\Sigma_{1/2}\rangle \\ &= \langle {}^2\Sigma_{-1/2}|\mathbf{L}^{+}|{}^2\Pi_{-3/2}\rangle \\ &= \langle {}^2\Pi_{-3/2}|\mathbf{L}^{-}|{}^2\Sigma_{-1/2}\rangle = L_{\Pi,\Sigma}. \end{aligned} \tag{58}$$

The direction cosine matrix elements along the space-fixed Z-axis can be obtained from Hougen's table [36].

The non-vanishing matrix elements of $H_{\rm Z}$ in the Radford-Broida basis set then are:

$$\langle 1, c, J, M|H_{\rm Z}|1, c, J, M\rangle = -\frac{M}{J+1}\mu_{\rm B}\mathcal{H} \tag{59}$$

$$\langle 1, d, J, M|H_{\rm Z}|1, d, J, M\rangle = \frac{M}{J}\mu_{\rm B}\mathcal{H} \tag{60}$$

$$\begin{aligned} \langle 2, c/d, J, M|H_{\rm Z}|2, c/d, J, M\rangle = \Big[\left(1+\frac{g_{\rm S}}{2}\right)a^2\frac{3M}{J(J+1)} \\ + 2g_{\rm S}abtM\Big]\mu_{\rm B}\mathcal{H} \end{aligned} \tag{61}$$

$$\begin{aligned} \langle 3, c/d, J, M|H_{\rm Z}|3, c/d, J, M\rangle = \Big[\left(1+\frac{g_{\rm S}}{2}\right)b^2\frac{3M}{J(J+1)} \\ - 2g_{\rm S}abtM\Big]\mu_{\rm B}\mathcal{H} \end{aligned} \tag{62}$$

$$\begin{aligned} \langle 1, c/d, J, M|H_{\rm Z}|2, c/d, J, M\rangle = -2^{-1/2}L_{\Pi,\Sigma}M(at \mp bu) \\ \times \mu_{\rm B}\mathcal{H} \end{aligned} \tag{63}$$

$$\begin{aligned} \langle 1, c/d, J, M|H_{\rm Z}|3, c/d, J, M\rangle = -2^{-1/2}L_{\Pi,\Sigma}M(bt \pm au) \\ \times \mu_{\rm B}\mathcal{H} \end{aligned} \tag{64}$$

$$\begin{aligned} \langle 2, c/d, J, M|H_{\rm Z}|3, c/d, J, M\rangle = (b^2-a^2)g_{\rm S}t\mu_{\rm B}\mathcal{H} \\ + ab(1+\frac{g_{\rm S}}{2})\frac{3M}{J(J+1)}\mu_{\rm B}\mathcal{H} \end{aligned} \tag{65}$$

with

$$t \equiv \frac{[J(J+1) - 3/4]^{1/2}}{J(J+1)}, \tag{66}$$

$$u \equiv \frac{(J+1/2)}{J(J+1)}c/d \tag{67}$$

Note that the off-diagonal Zeeman matrix elements (63, 65) modify the field-free perturbations given by the matrix elements (43, 45). Also, note that states with the same c/d symmetry have the same parity but not *vice versa*.

Apart from the matrix elements that connect states with same J and M there are non-vanishing matrix elements between states with same M and parity but with J's that differ by $\Delta J = \pm1$. These matrix elements

$$\begin{pmatrix} \langle 1,c,J-1,M|H|1,c,J-1,M\rangle & \langle 1,c,J-1,M|H|1,d,J,M\rangle & \langle 1,c,J-1,M|H|3,d,J,M\rangle \\ \langle 1,d,J,M|H|1,c,J-1,M\rangle & \langle 1,d,J,M|H|1,d,J,M\rangle & \langle 1,d,J,M|H|3,d,J,M\rangle \\ \langle 3,d,J,M|H|1,c,J-1,M\rangle & \langle 3,d,J,M|H|1,d,J,M\rangle & \langle 3,d,J,M|H|3,d,J,M\rangle \end{pmatrix} \quad (68)$$

have always to be included for the other member of the Σ-doublet since members of a Σ-doublet are quasi-degenerate and have the same parity. On the other hand, in the case of a large spin-orbit splitting between the $^2\Pi_{|1/2|}$ and $^2\Pi_{|3/2|}$ states (or, more accurately, large λ), there can only be a significant interaction between the $^2\Sigma_{|1/2|}$ state and just one of the $^2\Pi$ states (the one that exhibits an accidental quasi-degeneracy with the $^2\Sigma_{|1/2|}$ state). Therefore, the Hamiltonian can be well approximated by a 3×3 matrix built out of elements that connect the Σ-doublet with either the $^2\Pi_{|1/2|}$ or the $^2\Pi_{|3/2|}$ state. Note that the other member of the $^2\Pi_{|1/2|}$ or $^2\Pi_{|3/2|}$ Λ-doublet does not interact with the three states because of its different parity.

Thus, in the case of a quasi-degeneracy, for given vibronic states and a given J, between the $|1,d,J,M\rangle$ and $|3,d,J,M\rangle$ states of negative parity, the 3×3 Hamiltonian matrix will also have matrix elements due to the $|1,c,J-1,M\rangle$ state:

see matrix (68) above.

The mixed-J matrix elements occur only for the Zeeman part of the Hamiltonian. For the above case these are:

$$\langle 1,c,J-1,M|H|1,d,J,M\rangle = g_{\rm S}\frac{[(J+1/2)(J-1/2)(J+M)(J-M)]^{1/2}}{J[(2J+1)(2J-1)]^{1/2}}\mu_{\rm B}\mathcal{H} \quad (69)$$

$$\langle 1,c,J-1,M|H|3,d,J,M\rangle = 2^{-1/2}L_{\Pi,\Sigma}a\frac{[(J+1/2)(J-1/2)(J+M)(J-M)]^{1/2}}{J[(2J+1)(2J-1)]^{1/2}}\mu_{\rm B}\mathcal{H} + 2^{-1/2}L_{\Pi,\Sigma}b\frac{[(J+3/2)(J+1/2)(J+M)(J-M)]^{1/2}}{J[(2J+1)(2J-1)]^{1/2}}\mu_{\rm B}\mathcal{H}. \quad (70)$$

5.3 Comparison of theory and experiment

Figure 20 shows the measured (points) spectral shifts (as derived from the positions of the maxima of the distribution curves of Fig. 13) as a function of the magnetic field strength at the edge of the trap, $\mathcal{H}_{\rm edge}$. The shifts are linear in field strength and correspond to a small difference ($0.02\,\mu_{\rm B}$) in the magnetic moments between the ground and excited states. Taking the field-free parameters of CaH from Berg and Klyning [27] and Martin [28] (see caption) and approximating $L_{\Pi,\Sigma} \equiv \langle\Pi|\mathbf{L}^+|\Sigma\rangle$ by $2\langle\Pi|\mathbf{BL}_y|\Sigma\rangle/B_\Sigma \equiv 2Q/B_\Sigma$ we obtained Zeeman curves for the $N'=1$, $J'=3/2$, $M'=\pm3/2$ that, after subtraction of the respective $N''=0$, $J'=1/2$, $M'=\pm1/2$ curves, yield a qualitative agreement with the observed Zeeman shifts (dashed lines). The positive Zeeman shift corresponds to the transition between the $N''=0, J''=1/2, M''=1/2$ and the $N'=1, J'=3/2, M'=3/2$ state, and the negative shift to the transition between the $N''=0, J''=1/2, M''=-1/2$ and the $N'=1, J'=3/2, M'=-3/2$ state. By fitting the calculated Zeeman shifts to the observed ones (full lines) we obtain $L_{\Pi,\Sigma}=0.4$. This value is about twice that of $2Q/B_\Sigma$, *i.e.* quite at odds with the "pure precession" hypothesis, see, *e.g.*, [37]. The analysis of extensive field-free spectra of CaH [27,28] led earlier to a similar conclusion.

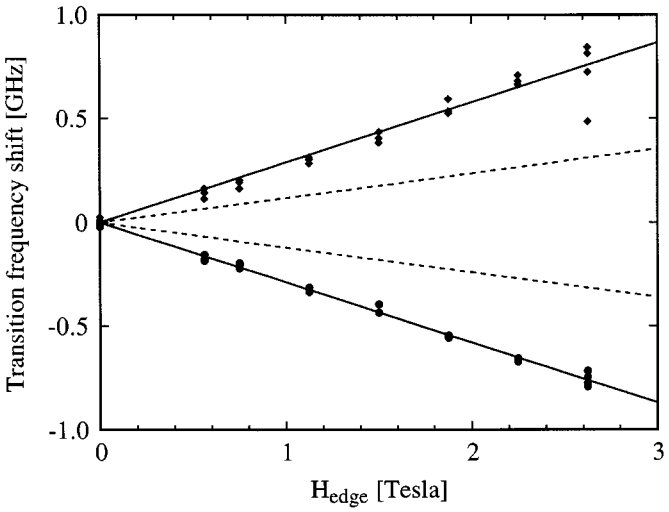

Fig. 20. Measured (points) spectral shifts as a function of the magnetic field strength at the edge of the trap. The dashed lines show a simulation based on an estimate of the $\langle\Pi|\mathbf{L}^+|\Sigma\rangle$ coupling between the $B, v'=0$ and $A, v'=1$ states, the full line is a fit to the experimental data yielding $\langle\Pi|\mathbf{L}^+|\Sigma\rangle=0.4$, see text.

The calculated slope of the negative Zeeman shift is slightly steeper than that of the positive shift; this is due to the enhanced repulsion of the $N'=1, J'=3/2, M'=3/2$ state that lies closer to the perturbing A-state.

Table 1. Examples of trap parameters of species confined in a buffer-gas loaded magnetic trap. See text.

Species	State	Buffer gas	T [mK]	κ	$\langle\mu\rangle$ [μ_B]	$\mathcal{H}_{edge}$ [T]	η	N
^{52}Cr	$^7S_3$	^{3}He	300	~ 10	~ 6	0.7	~ 9	$\sim 10^{11}$
		^{4}He	1,400	~ 8	~ 6	2.4	~ 7	$\sim 10^{11}$
^{151,153}Eu	$^8S_{7/2}$	^{3}He	250	~ 26	~ 7	0.6	~ 11	$\sim 10^{12}$
		^{4}He	800	~ 20	~ 7	2.0	~ 12	$\sim 10^{12}$
^{40}Ca^{1}H	$^2\Sigma^+$	^{3}He	400	~ 8	~ 1	3.0	~ 5	$\sim 10^8$

6 A retrospect

Table 1 gives an overview of the characteristic parameters of buffer-gas loaded magnetic traps used in our Cr, Eu, and CaH experiments. In the above work neither the production method (laser ablation) nor the magnetic trapping field (an anti-Helmholtz setup) were optimized. And yet, the initial numbers of the atomic species were about 100 fold of those achieved with alkali metals in MOT's. The lifetime of the atomic species in the trap was primarily limited by two-body decay. The decay of CaH was primarily one-body, corresponding to evaporation over the trap edge due to a low value of the η parameter.

7 Prospects

7.1 Atoms

Most of the interest, both experimental and theoretical, in atom trapping has been directed toward bosons. This is mainly due to the rarity of fermionic isotopes among alkali metals. Stable fermions are generally rarer than bosons (because of the relation between the symmetry nature of the atom and the stability of the nucleus) but the periodic table is still teeming with them, see Figure 1. Buffer-gas loaded magnetic traps may make it now possible to explore a wide variety of ultracold fermionic gases.

A number of new phenomena have been identified in ultracold fermionic gases, including ultrastability, linewidth narrowing, and superfluidity. Most of these phenomena are easier to observe with larger numbers of atoms. This is not only due to the obvious advantage of an increased signal-to-noise ratio, but also due to a higher Fermi energy.

Ultrastability arises in a weakly interacting ensemble of fermions due to the antisymmetrization requirement that prevents the fermions from approaching one another at distances much smaller than the local de Broglie wavelength. As a result, at low enough temperatures fermions interact by the long-range part of their interaction potential only and so their inelastic scattering cross-sections are suppressed. The work of Koelman *et al.* [12] showed that a Fermi gas would persist in a single fine or hyperfine (trappable) state while the relatively less suppressed elastic collisions would ensure thermal equilibrium.

A signature of the Fermi degenerate regime could be the decrease of the decay rate of electronically excited atoms. The resulting linewidth narrowing is caused by a reduction, due to particle symmetry, of the phase space into which the excited fermions can decay. Although a high optical density may lead to complications, it might be possible to produce linewidths narrower than the natural linewidth, a dramatic effect indigenous to the Fermi degenerate regime [38–40].

Attaining superfluidity (corresponding to a macroscopic wavefunction of Cooper pairs on the Fermi surface) is another tantalizing prospect for fermions [41,42].

An advantage offered by buffer-gas loaded magnetic traps over MOT's is the ease of extending trapping to other species as well as the large number of atoms (or molecules) trapped. Buffer-gas loading also may allow the loading of multiple isotopes [21], and should easily make possible the loading of multiple species. In order to cool the sample below the loading temperature, evaporative cooling can be employed. With a given initial number of atoms, the lowest temperature attainable by evaporative cooling is limited by the ratio of the rate at which the atoms redistribute their energy by elastic collisions to the dipolar relaxation rate. The low-temperature elastic scattering cross-sections vary greatly among species. For instance, for atomic hydrogen the cross-section is smaller by a factor of several thousand than for alkali metals. However, there are reasons to believe that the alkali-hydrogen elastic cross-section is comparable to that for the alkali-alkali scattering. Consequently, seeding hydrogen with alkali, or possibly chromium, atoms would enormously enhance the thermalization rate [43]. The result may be much larger condensates produced in a much shorter time. Similarly, the ability to load multiple isotopes should be of great advantage in attempts to evaporatively cool fermionic isotopes. For instance, in the case of chromium, ^{53}Cr is a fermion (nuclear spin = 3/2) and ^{52}Cr is a boson (nuclear spin 0). Chromium offers the possibility of easy loading of the necessary isotopes at high densities. Then the bosonic ^{52}Cr could be used to thermalize, and hence cool, ^{53}Cr. It remains to be seen, however, whether the low-temperature elastic and two-body relaxation cross-sections will be favorable enough for reaching the quantum degenerate regime.

7.2 Molecules

Trapping of molecules should prove particularly useful in spectroscopy and the study of molecular structure, especially in ultra-high resolution spectroscopy that requires cold (slow), trapped (long interaction time) samples.

One of the proposed candidates for use in the search for an elementary electric dipole moment (EDM, a test of time reversal symmetry) [44,45] is YbF. High-resolution spectroscopic experiments carried out so far probe hot YbF molecules prepared by thermal dissociation of a precursor. However, using buffer-gas cooled YbF instead could dramatically increase the sensitivity of the EDM search [46]. Since the ground-state electronic structure lends YbF a $1\,\mu_{\rm B}$ dipole moment, such enhanced search experiment appears feasible. Other paramagnetic molecules are also the subject of investigation for use in experiments testing both parity and time reversal violation [47].

Trapping of molecules should in general be beneficial to high resolution spectroscopy. For instance, trapped molecules could be used to study highly forbidden transitions. Also, the long interaction time available could make it easier to tailor the internal wavefunctions of the molecules using external fields and thus become a tool of coherent control. The technique should also enable the study of interactions of ultra-cold gases of molecules whose axes could, in some cases, be spatially oriented [48–51]. This would enhance the dynamical resolution of many spectroscopic and collisional experiments since it eliminates averaging over random spatial orientations. Such polarization is possible when the electronic Hamiltonian possesses nonzero diagonal elements in Hund's case (a) or (c) bases.

The creation of low-temperature samples of molecules may allow loading of the far-off-resonance optical trap [52,53]. The use of the FORT provides the additional possibility of doing spectroscopy with no magnetic field present. It may be possible to use buffer-gas loading to fill a FORT directly with molecules [54] or by transfer from a buffer-gas loaded magnetic trap. Trapping in a FORT of translationally cold (but vibrationally and rotationally hot) Cs_2 prepared by photoassociation has recently been reported [55].

There is extensive interest in the very low energy collisional relaxation of molecules [56–60]. The production of ultra-cold molecules would allow the study of collisions where the translational energy is smaller than the other relevant energy scales in the system. The technique offers the possibility of investigating low-temperature collisional relaxation processes from excited electronic and rovibrational states. In addition to providing fundamental information on the interaction of molecules, these studies would also determine the feasibility of loading atoms and molecules in very long-lived metastable states.

The technique may also enable the study of collective quantum effects in molecular systems, both bosonic and fermionic. It is known that the efficacy of evaporative cooling depends critically on the ratio of the dipolar relaxation cross-section to the elastic cross-section. There is an extreme sensitivity of this ratio to subtle details of the interaction potential. The effects of these cross-sections on the behavior of a molecular Bose condensate or a Fermi degenerate gas is an open question [61–63]. Using a variety of different molecules to form ultracold gases could help understand these new forms of matter.

This material is based upon work supported by the National Science Foundation under Grant No. PHY-9511951. J.D.W. is supported by a National Science Foundation Graduate Research Fellowship.

Appendix

The Zeeman Hamiltonian of an atom with electronic spin and orbital angular momenta $\mathbf{S}$ and $\mathbf{L}$ and a zero nuclear spin subject to a magnetic field $\mathcal{H}$ takes the form [64]:

$$H = g_{\rm J}\mu_{\rm B}\mathbf{J}\cdot\mathcal{H} \tag{A.1}$$

where $\mathbf{J}$ is the total electronic angular momentum of the atom, $g_{\rm J}$ the corresponding g-factor, and $\mu_{\rm B}$ the Bohr magneton. The matrix elements of H can be obtained analytically, either in the coupled basis, $|J,M\rangle$, corresponding to the weak-field limit, or in the uncoupled basis, $|M_{\rm L},M_{\rm S}\rangle$, corresponding to the strong-field limit (Paschen-Back uncoupling). Hence either yields the eigenenergies and line strengths in closed form.

A.1 Low-field limit

In the low-field limit, the angular momenta $\mathbf{S}$ and $\mathbf{L}$ couple to a resultant total angular momentum $\mathbf{J}=\mathbf{S}+\mathbf{L}$ characterized by a quantum number $J = L+S, L+S-1, ..., |L-S|$; each value of J has $2J+1$ projections $M = -J, -J+1, ..., +J$ on the space-fixed axis defined by the direction of $\mathcal{H}$. Note that there are $\sum_J(2J+1) = (2L+1)(2S+1)$ coupled states $|J,M\rangle$. The eigenenergy is given by [64]

$$E(J,M) = Mg_{\rm J}\mu_{\rm B}\mathcal{H} \tag{A.2}$$

where

$$g_{\rm J} = g_{\rm L}\frac{J(J+1)+L(L+1)-S(S+1)}{2J(J+1)} + g_{\rm S}\frac{J(J+1)+S(S+1)-L(L+1)}{2J(J+1)} \tag{A.3}$$

S and L are the total electronic spin and orbital angular momentum quantum numbers, and $g_{\rm L}=1$ and $g_{\rm S}\cong 2.0023$ are the orbital and spin gyromagnetic ratios of the electron; $\mathcal{H}\equiv|\mathcal{H}|$.

The line strength factor $S_q(L'S'J'M';LSJM)$ of a transition between states $|L'S'J'M'\rangle \leftarrow |LSJM\rangle$ due to an electric dipole moment d_q (of unit magnitude, with $q=0$ for parallel and $q=\pm1$ for perpendicular transitions) is given by [65]

$$S_q = |\langle L'S'J'M'|d_q|LSJM\rangle|^2 \tag{A.4}$$

with

$$\langle LSJM|d_q|L'S'J'M'\rangle = (-1)^{2J-M'+L'+S+1}[(2J+1)(2J'+1)]^{1/2} \times \begin{pmatrix} J & 1 & J' \\ -M & q & M' \end{pmatrix} \begin{Bmatrix} L & 1 & J \\ J' & S & L \end{Bmatrix} \langle L||d||L'\rangle. \tag{A.5}$$

A.2 Strong-field limit

In the strong-field limit, the angular momenta **L** and **S** are no longer integrals of motion but their projections $M_{\rm L}$ and $M_{\rm S}$ on the space-fixed axis are. Since $M_{\rm L}$ and $M_{\rm S}$ take respectively $(2L+1)$ and $(2S+1)$ values, there are $(2L+1)(2S+1)$ uncoupled states $|M_{\rm L}, M_{\rm S}\rangle$. In the uncoupled basis, the eigenvalues of Hamiltonian (A.1) are given by [64]

$$E(M_{\rm L}, M_{\rm S}) = M_{\rm L} g_{\rm L} \mu_{\rm B} \mathcal{H} + M_{\rm S} g_{\rm S} \mu_{\rm B} \mathcal{H}. \quad \text{(A.6)}$$

The line strength factor $S_q(M'_{\rm L}, M'_{\rm S}; M_{\rm L}, M_{\rm S})$ of a transition between states $|M'_{\rm L}, M'_{\rm S}\rangle \leftarrow |M_{\rm L}, M_{\rm S}\rangle$ due to an electric dipole moment d_q (of unit magnitude, with $q = 0$ for parallel and $q = \pm 1$ for perpendicular transitions) is given by [65]

$$S_q = |\langle M'_{\rm L}, M'_{\rm S}|d_q|M_{\rm L}, M_{\rm S}\rangle|^2 \quad \text{(A.7)}$$

with

$$\langle M'_{\rm L}, M'_{\rm S}|d_q|M_{\rm L}, M_{\rm S}\rangle = (-1)^{L-M_{\rm L}} \delta(M'_{\rm S}, M_{\rm S}) \times \begin{pmatrix} L & 1 & L' \\ -M_{\rm L} & q & M'_{\rm L} \end{pmatrix} \langle L||d||L'\rangle. \quad \text{(A.8)}$$

A.3 Populations and intensities

The initial field-free populations, $P(J)$, of an J-state at a temperature T are given by

$$P(J) = (2J+1) \exp\left(-\frac{E_{\rm J}}{kT}\right). \quad \text{(A.9)}$$

In the high-field limit, the populations of the $|M_{\rm L}, M_{\rm S}\rangle$ states are determined by adiabatic transfer of the low-field populations of the $|J, M\rangle$ states which, in turn, is given by the transformation of the coupled to the uncoupled basis [30]:

$$P(M_{\rm L}, M_{\rm S}) \propto \langle LM_{\rm L}, SM_{\rm S}|JM\rangle^2 = (2J+1) \begin{pmatrix} L & S & J \\ M_{\rm L} & M_{\rm S} & -M \end{pmatrix}^2. \quad \text{(A.10)}$$

The correlation between the low- and high-field limits is determined by the non-vanishing 3-J symbols. The intensities, $\mathcal{I}$, of the transitions between states in absorption or excitation spectra are then given by

$$\mathcal{I}(M'_{\rm L}, M'_{\rm S}; M_{\rm L}, M_{\rm S}) \propto P(M_{\rm L}, M_{\rm S}) S(M'_{\rm L}, M'_{\rm S}; M_{\rm L}, M_{\rm S}). \quad \text{(A.11)}$$

References

1. W. Ketterle, N.J. van Druten, Adv. At. Mol. Opt. Phys. **37**, 181 (1996).
2. B. Friedrich, R. deCarvalho, J. Kim, D. Patterson, J.D. Weinstein, J.M. Doyle, J. Chem. Soc., Faraday Trans. **94**, 1783 (1998).
3. J.M. Doyle, B. Friedrich, J. Kim, D. Patterson, Phys. Rev. A **52**, R2515 (1995).
4. J.R. Heath, Q.L. Zhang, S.C. O'Brien, R.F. Curl, H.W. Kroto, R.E. Smalley, J. Am. Chem. Soc. **109**, 359 (1987).
5. J. Wilks, in *The Properties of Liquid and Solid Helium* (Clarendon Press, Oxford, 1987); vapor pressure of ^{4}He is determined from extrapolation of data given in this reference.
6. J. Res. Nat. Bureau Stds. A Phys. Chem. A **68**, 579 (1964), densities of ^{3}He gas are determined from extrapolation of data present in this reference.
7. J.M. Doyle, Ph.D. thesis, MIT, 1991.
8. W. Petrich, M.H. Anderson, J.R. Ensher, E.A. Cornell, Phys. Rev. Lett. **74**, 3352 (1995).
9. J.D. Weinstein, R. deCarvalho, J. Kim, D. Patterson, B. Friedrich, J.M. Doyle, Phys. Rev. A **57**, R3173 (1998).
10. W. Ketterle, K.B. Davis, M.A. Joffe, A. Martin, D.E. Pritchard, Phys. Rev. Lett. **70**, 2253 (1993).
11. J.M.V.A. Koelman, H.T.C. Stoof, B.J. Verhaar, J.T.M. Walraven, Phys. Rev. Lett. **59**, 676 (1987).
12. J.M.V.A. Koelman, H.T.C. Stoof, B.J. Verhaar, J.T.M. Walraven, Phys. Rev. B **38**, 9319 (1988).
13. M. Houbiers, R. Ferwerda, H.T.C. Stroof, W.I. McAlexander, C.A. Sockett, R.G. Hulet, Phys. Rev. A **56**, 4864 (1997).
14. J. Javanainen, J. Ruostekoski, Phys. Rev. A **52**, 3033 (1995).
15. V. Sandoghar *et al.*, J. Mod. Opt. **44**, 1883 (1997).
16. J.J. McClelland, W.R. Anderson, R.J. Celotta, Proc. SPIE Int. Soc. Opt. Eng. **2995**, 90 (1997).
17. C.E. Moore, in *Atomic Energy Levels As Derived From the Analyses of Optical Spectra* (National Bureau of Standards, USA, 1971), Volume II.
18. T. Reinhardt, J. Maichel, M. Baumann, J. Krueger, Z. Phys. D **34**, 87 (1995).
19. J. Kim, Ph.D. thesis, Harvard University, 1997.
20. D.W. Sedgley, A.T. Tobin, T.H. Batzer, W.R. Call, J. Vac. Sci. Tech. A **5,** 2572 (1987).
21. J. Kim, B. Friedrich, D.P. Katz, D. Patterson, J.D. Weinstein, R. deCarvalho, J.M. Doyle, Phys. Rev. Lett. **78**, 3665 (1997).
22. K.B. Blagoev, V.A. Komarovskii, At. Nucl. Data Tables **56**, 1 (1994).
23. G.J. Zaal, W. Hogerworst, E.R. Eliel, K.A.H. van Leeuwen, J. Blok, Z. Phys. A **290**, 339 (1979).
24. N.F. Ramsey, in *Molecular Beams* (Oxford University Press, London, 1955).
25. *Experimental Transition Probabilities for Spectral Lines of Seventy Elements, NBS53* (US Department of Commerce, NBS, 1962).
26. J. Weinstein, R. deCarvalho, T. Guillet, B. Friedrich, J.M. Doyle, Nature **395**, 148 (1998).
27. L.E. Berg, L. Klyning, Phys. Scripta **10**, 331 (1974).
28. H. Martin, J. Mol. Spect. **108**, 66 (1984).
29. T. Leininger, G. Jeung, J. Chem. Phys. **103**, 3942 (1995).
30. R.N. Zare, *Angular momentum* (Wiley, New York, 1988).

31. B. Friedrich, R. deCarvalho, J.D. Weinstein, J.M. Doyle, J. Chem. Phys. **110**, 2376 (1999).
32. G. Herzberg, *Spectra of diatomic molecules* (van Nostrand, Princeton, 1950).
33. H.E. Radford, H.P. Broida, Phys. Rev. **128**, 231 (1962).
34. J.H. van Vleck, Phys. Rev. **33**, 467 (1929).
35. H. Lefebvre-Brion, R.W. Field, *Perturbations in the spectra of diatomic molecules* (Academic Press, New York, 1986).
36. J.T Hougen, *The calculations of rotational energy levels and rotational line intensities in diatomic molecules* (National Bureau of Standards Monograph 115, Washington, 1970).
37. H.E. Radford, Phys. Rev. **126**, 1035 (1962).
38. M. Gross, S. Haroche, Phys. Rep. **93**, 301 (1982).
39. C. Cohen-Tannoudji, J. Dupont-Roc, G. Grynberg, *Atom-Photon Interactions, Basic Processes and Applications* (Wiley, New York, 1992).
40. J. Javanainen, J. Ruostekoshi, Phys. Rev. A **52**, 3033 (1995).
41. A. Legget, J. Phys. Colloq. France **41**, C7-19 (1980).
42. M. Houbier, R. Ferwerda, H. Stoof, W. McAlexander, C. Sackett, R. Hulet, Phys. Rev. A **56**, 4864 (1997).
43. D. Kleppner (private communication).
44. M.G. Kozlov, V.F. Ezhov, Phys. Rev. A **49**, 4502 (1994).
45. E.A. Hinds, K. Sangster, AIP Conf. Proc., **270**, 77 (1993).
46. B.E. Sauer, J. Wang, E.A. Hinds, Bull. Am. Phys. Soc. Ser. II, **39**, 1060 (1994).
47. B.N. Ashkinadzi, V.F. Ezhov, M.N. Groshev, V.V. Jaschuk, A.Yu. Khazov, V.A. Knjazkov, M.G. Kozlov, V.L. Riabov, M.A. Yugaldin, Preprint from the Russian Academy of Sciences, St. Petersburg, 1994.
48. B. Friedrich, D. Herschbach, Z. Phys. D **18**, 153 (1991).
49. B. Friedrich, D. Herschbach, Nature **353**, 412 (1991).
50. B. Friedrich, D. Herschbach, Z. Phys. D **24**, 25 (1992).
51. B. Friedrich, A. Slenczka, D. Herschbach, Can. J. Phys. **72**, 897 (1994).
52. J.D. Miller, R.A. Cline, D.J. Heinzen, Phys. Rev. A **47**, R4567 (1993).
53. W.D. Philips, in *Laser Manipulation of Atoms and Ions*, edited by E. Arimondo, W. Philips, F. Sturmia, School of Atomic Physics "Enrico Fermi", Course CXVIII (North Holland: Amsterdam, 1992), pp. 334-335.
54. B. Friedrich, D. Herschbach, Phys. Rev. Lett. **74**, 4623 (1995).
55. T. Takekoshi, B.M. Patterson, R.J. Knize, Phys. Rev. Lett. (in press, 1998).
56. D.W. Noid, S.K. Gray, S.A. Rice, J. Chem. Phys. **84**, 2649 (1986).
57. S.K. Gray, S.A. Rice, J. Chem. Phys. **83**, 2818 (1985).
58. J.T. Bahns, P.L. Gould, W.C. Stwalley, J. Chem. Phys. **104**, 9689 (1996).
59. N. Balakrishnan, V. Kharchenko, R.C. Forrey, A. Dalgarno, Phys. Rev. Lett. **80**, 3224 (1998).
60. R.C. Forrey, N. Balakrishnan, V. Kharchenko, A. Dalgarno, Phys. Rev. A **58**, R2645 (1998).
61. M.H. Anderson, J.R. Ensher, M.R. Matthews, C.E. Wieman, E.A. Cornell, Science **269**, 198 (1995).
62. K.B. Davis, M.-O. Mewes, M.R. Andrews, N.J. van Druten, D.S. Durfee, D.M. Kurn, W. Ketterle, Phys. Rev. Lett. **76**, 3969 (1995).
63. C.C. Bradley, C.A. Sockett, R.G. Hulet, Phys. Rev. Lett. **78**, 985 (1997).
64. G. Herzberg, *Atomic Spectra and Atomic Structure* (Dover, New York, 1945).
65. B.W. Shore, *The Theory of Coherent Atomic Excitation* (Wiley, New York, 1990).